Non-equilibrium lattice dynamics of THz-driven polar semiconductors from first principles

Masters Thesis in the Computational Solid-State Theory group of
Prof. Caruso at Christian-Albrechts-Universität Kiel

Mate Ćapin
Matrikelnummer: 1112086
stu204503@mail.uni-kiel.de
Handed in: 22.12.2022

1. Gutachter: Prof. Dr. Fabio Caruso
2. Gutachter: Prof. Dr. Michael Bauer

Table of Contents

Abstract

Non-equilibrium dynamics determine a wide range of properties of solid structures. Through phonon dynamics for example thermoelectric processes, as well as the electric and thermal transport are determined. These properties are important in the development of new technologies in a number of industries and for research alike.

In this work first-principles are used to calculate the structure and phonon thermalisation of polar semiconductors, using the time-dependent Boltzmann equation. Considering out of equilibrium states, excited by infrared absorption sets the need for a time-dependent description of the dynamics. These ab-initio calculations are set up in this work with Tungsten-Disulfide as an example material. The procedure to achieve ideal results and analyse the phonon scattering and lattice thermalisation is transferable to other composites.

Zusammenfassung

Die Nichtgleichgewichtsdynamik bestimmt eine vielzahl an Eigenschaften von Festkörpern. Die dynamischen Prozesse der Phononen zum Beispiel bestimmen unter Anderem thermoelektrische Prozesse, oder elektrische und thermische Leitfähigkeit. Diese Eigenschaften sind für die Entwicklung neuer Technologien in einer Reihe von industriellen Branchen, sowie in der Forschung von Bedeutung.

In dieser Arbeit werden first-principles Berechnungen genutzt, um die Struktur und Thermalisierung von polaren Halbleitern unter Verwendung der zeitabhängigen Boltzmann-Gleichung zu berechnen. Eine Betrachtung von Zuständen außerhalb des Gleichgewichtszustandes, angeregt durch die Absorption infraroter Strahlung erfordert eine zeitabhängige Beschreibung der Dynamik im Festkörper. Diese ab-initio-Rechnungen werden hier mit Wolfram-Disulfid als Beispielmaterial durchgeführt. Der Prozess, um zu den idealen Parametern für die Berechnungen zu gelangen und die Analyse der Phononenstreuung ist auf andere Materialien übertragbar.

1 Introduction

The phononic system is a well known subject in the field of solid state physics. Both theory and experiment have provided a wide variety of data and concepts surrounding it. But there is still a sizeable amount of unexplored possibilities and opportunities for an expansion of the theory of vibrational modes and the processes within.

Solid-state technologies often depend on the dynamics of electrons, phonons and excited states in the underlying systems. Important properties like the electronic transport are limited by the scattering of charge carriers with phonons and defects [1]. The phonon-phonon scattering is the key component for heat transport and thermoelectric processes [2, 3]. These dynamical processes take place on nanosecond timescales and involve complicated experimental setups to realise the time resolution needed to investigate [4, 5, 6] . This underlines the importance of an elaborate theory of solids and their properties, as this would allow for experimental outcomes to be predicted, consequentially automatically ruling out experiments that would not lead to good results.

Recently first principles simulations were evolved to enable an accurate calculation of electron phonon interactions without heuristic parameters. This opens the door for new approaches to investigate the properties of solids and provides vast possibilities for research in electronics, optoelectronics, and renewable energy [7, 8], leading to further development in the underlying codes and theories.

The material examined in this work belongs to the group of transition metal dichalcogindes (TMDs). This group of semiconductors is a popular subject of research due to their beneficial properties for different departments of electronics [9, 10, 11], like the field effect transistor, or sensing [12], as replacement for graphene. For most of the possible operation areas monolayers are needed. In the case of TMDs this monolayer is atomically thin, which is why they are called 2-dimensional. In this work Tungsten-Disulfide will be investigated, which is used for low friction applications, as material for gears, or as a lubricant in motoroils [13, 14] .

This work aims to expand the theory of light absorption and the subsequent relaxation of the lattice in polar semi-conductors via first principle calculations with Tungsten-Disulfide (WS_2) as example material. The main subject of research are the relaxation processes of the phononic system after an excitation through infrared photons. These processes are examined by performing calculations with multiple simulation codes, setting the crystalline structure, simulating an infrared excitation and subsequently examining the thermal relaxation. The crystal structure will be set up and relaxed via Quantum Espresso. Afterwards an excitation by infrared photons will be introduced to the grid, leading to heating of the phonon modes excited. Subsequently the relaxation of the excitation into other vibrational modes is calculated with ShengBTE and investigated by post-processing the output data.

Using first principles has only been a real possibility with the rapid rise in computational power over the last few decades. With this development a rigid structure of restrictions and rules can be introduced to calculate the physical properties of complex systems, such as the one investigated here. The simulation in timescales of tens of picoseconds and a time resolution within the range of femtoseconds was developed rather recently. In this work first-principles and electron phonon interactions are combined with a parallel numerical calculation to propagate the Boltzmann equations in time, providing insight into the scattering mechanisms underlying the thermalisation of the grid. The time dependent Boltzmann equation is used due to the time dependent nature of the processes. The scattering process due to infrared excitation drives the lattice out of equilibrium, which is then restored after a certain time. Other works employ similar techniques to characterise different properties [5], including the coupled dynamic degrees of freedom for electrons and nucleons [15, 16], the manipulation of ultrafast structural dynamics [17, 18], or phase transitions [19]. In this work the lattice experiences decay of phonons only, electrons do not play a part here and can be assumed to be frozen in place.

In the first part of this work the computational and theoretical basis will be given, followed by a detailed description of the methodology used to achieve the results. Here the simulation codes will be described and the important parameters as well as their possible values will be addressed. The results presented in the subsequent chapter are obtained by these simulations. Finally a summary will be given, along with an outlook on further possible research on this topic.

2 Theory

Atoms, molecules and three-dimensional solids consist of the same building blocks, namely a finite number of indistinguishable electrons and nucleons. In the first-principles description of many-body systems the physical properties are determined without experimental data, which requires a solid and elaborate theoretical basis in which approximations should be introduced only if they are justified and do not take away any underlying properties. First-principles calculations aim to extend the Density Functional Theory (DFT) and the related excited state methods [20], but are still in an early state of development. In general there are two main ways of approaching the calculations. First the real-time time-dependent DFT [21], which uses the Kohn-Sham Hamiltonian to self-consistently achieve a time propagation of the electronic wavefunction and charge density [22]. Secondly the many-body perturbation theory is used to compute the electron-electron, electron-phonon and phonon-phonon interaction. In combination with the Boltzmann Transport Equation (BTE) the dynamics and the transport in solids and the dynamic properties of the crystal can be investigated and quantified.

2.1 Density Functional Theory

Every system of particles can be described exactly by the corresponding wavefunction $\Psi_s = \Psi_s(\mathbf{r},\sigma,\mathbf{R},\Sigma,t)$. This is a function of all the degrees of freedom of the structure, with $\mathbf{r}$ and $\mathbf{R}$ as the coordinates of electrons and nucleons respectively, and σ and Σ as their spin values. In the following the nuclear spin Σ will be neglected, as the effect on the crystal properties is negligible in this work. The s in the index denotes the eigenstate of the system.
First principles descriptions of the electronic structure of atoms, molecules and solids has peaked in the formulation of the Density Functional Theory (DFT) [23], as it is the foundation of most modern ab-initio calculations [7, 24]. In order to describe the structures of the systems in question the Schrödinger Equation is formulated, as solving it would yield the wavefunction. In the non-relativistic case the following relation is valid [25]:

$$\hat{H}\Psi_s = i\hbar\frac{\partial\Psi_s}{\partial t} \tag{2.1}$$

Here $\hat{H}$ is the Hamiltonian operator, $\hbar$ is the reduced Planck constant and i is the imaginary unit. The wavefunction undergoes partial derivation by the time t. The Hamiltonian consists of the following parts:

$$\hat{H} = \hat{T}_n + \hat{T}_e + \hat{V}_{nn} + \hat{V}_{ee} + \hat{V}_{en} \tag{2.2}$$

In this equation both the electronic and the nuclear kinetic terms $\hat{T}$ as well as the parts that consider Coulomb interactions $\hat{V}$ are included for both the nucleons (index n) and the electrons (index e). The kinetic parts are defined as follows [7]:

$$\hat{T}_n = -\sum_{I=1}^{N_n} \frac{\hbar^2 \nabla_I^2}{2M_I} \tag{2.3}$$

$$\hat{T}_e = -\sum_{i=1}^{N} \frac{\hbar^2 \nabla_I^2}{2m_e} \tag{2.4}$$

The indices I and i refer to the coordinates of the nucleon and electron respectively. The coulomb interaction is defined for electron-electron interactions, electron-nucleon interactions and nucleon-nucleon interactions, in the following way:

$$\hat{V}_{nn} = \frac{1}{2}\frac{e^2}{4\pi\varepsilon_0} \sum_{I=1}^{N_n} \sum_{\substack{J=1,\\ J\neq I}}^{N_n} \frac{Z_I Z_J}{|\mathbf{R}_I - \mathbf{R}_J|} \tag{2.5}$$

$$\hat{V}_{ee} = \frac{1}{2}\frac{e^2}{4\pi\varepsilon_0} \sum_{i=1}^{N_n} \sum_{\substack{i=1,\\ j\neq i}}^{N} \frac{1}{|\mathbf{r}_i - \mathbf{r}_i|} \tag{2.6}$$

$$\hat{V}_{en} = -\frac{e^2}{4\pi\varepsilon_0} \sum_{i=1}^{N} \sum_{I=1}^{N_n} \frac{Z_I}{|\mathbf{r}_i - \mathbf{R}_I|} \tag{2.7}$$

A solution to the Schrödinger Equation would provide a complete description of the system over time. However, due to the high number of degrees of freedom, especially when considering a big number of atoms like in solids, calculating the solution is virtually impossible as the computational cost rises exponentially with a higher number of degrees of freedom. Storing the wavefunction is one of the challenges [7].

Decoupling the electronic and nuclear parts of the Hamiltonian, as their dynamics happen on vastly different timescales, can be introduced. This is the Born Oppenheimer Approximation (BOA) which splits the SEq into two parts, the electronic and the nuclear SEq. Both of these can be solved separately by assuming that at each step in time the electrons follow the nuclear motion adiabatically. This in turn means that no transitions between different eigenstates of the electronic Hamiltonian can be triggered by the motion of the nucleons. The BOA is justified by the mass ratio of the nucleons and electrons: $\frac{\mathrm{m_n}}{\mathrm{m_e}} \approx 1837$ [26].

The approximation also implicates that for each timestep of the electron dynamics the nucleons can be approximated with fixed coordinates, which leads to an ansatz for the coupled electron-nuclear wavefunction in Dirac notation:

$$|\Psi\rangle = \sum_{\nu} |\psi_\nu\rangle \, |\chi_{\nu s}\rangle \tag{2.8}$$

Here ψ_ν is the eigenstate of the electronic Hamiltonian and $\chi_{\nu s}$ denotes functions of the nuclear coordinates. The latter depend on the nuclear coordinates $\mathbf{R}$ and the state of the system s as well as the electron quantum number ν. Both ψ_ν and $\chi_{\nu s}$ are solutions to the SEq and satisfy the requirements of orthogonality and normalisation, a probabilistic interpretation of the wavefunctions is thus possible.

With that the many-body wavefunction can be defined as a superposition of the many-electron and the many nuclei wavefunction [26]:

$$\Psi(r,R) = \sum_{\nu} \psi_\nu(r;R)\,\chi_\nu(R) \tag{2.9}$$

The electronic Hamiltonian and the electronic SEq are defined as follows:

$$\hat{H}_{\mathrm{el}}\,\Psi_\nu(r;R) = E_\nu \Psi(r;R) \tag{2.10}$$

$$\hat{H}_{\mathrm{el}} = \hat{T}_{\mathrm{e}} + \hat{V}_{\mathrm{ee}} + \hat{V}_{\mathrm{en}} \tag{2.11}$$

Here $\hat{V}_{\mathrm{en}}$ is the external potential which describes the effect that the nucleons have on the electrons. The electron-electron interactions described by the Coulomb term $\hat{V}_{\mathrm{ee}}$ is defined as follows:

$$\hat{V}_{\mathrm{ee}} = \sum_{\substack{i,j=1,\\ i\neq j}}^{N_{\mathrm{el}}} \frac{1}{|\hat{\mathbf{r}}_{\mathrm{i}} - \hat{\mathbf{r}}_{\mathrm{j}}|} \tag{2.12}$$

Due to the dependence of this expression on two coordinates and the need for a double sum the computational cost to calculate this property increases exponentially with the number of electrons (N_{el}). When describing a real system the computational cost exceeds the possibilities.

With a method introduced by Hohenberg, Kohn and Sham [23, 27] the exponential increase can be reduced to a linear increase with a rising number of electrons. For this a one-to-one correspondence of the electronic density and the ground-state wavefunction of the system is found. The electronic density [28] is defined as follows:

$$\hat{n}(\mathbf{r}) = \sum_{i=1}^{N_{\mathrm{el}}} \delta(\mathbf{r} - \hat{\mathbf{r}}_i) \tag{2.13}$$

The electrons are located at $\hat{\mathbf{r}}_i$. The delta-function reflects the discrete nature of the electron distribution. Using this term the electron-nucleon interaction can be rewritten:

$$\langle\psi|\hat{V}_{\mathrm{en}}|\psi\rangle = \int v_{\mathrm{en}}(r;R)\,n(\mathbf{r})\,d\mathbf{r} \tag{2.14}$$

The electron-nucleon interaction potential is the only parameter that depends on the nuclear coordinates and therefore holds the information about the properties of the entire system. The result is the needed one-to-one correspondence between the electronic density and the ground-state wavefunction. The first Hohenberg-Kohn Theorem states that for every electronic density there is exactly one corresponding electron-nucleon interaction potential. Due to this every quantity expressed by the wavefunction can equally be expressed by the electronic density. The ground state energy of a system can be written as [27]:

$$E[n] \; = \; F[n] + \int v_{\mathrm{en}}(\mathbf{r}; R)\, n(\mathbf{r}) d\mathbf{r} \tag{2.15}$$

$$F[n] \; = \; \langle \psi | \hat{T}_{\mathrm{e}} + \hat{V}_{\mathrm{ee}} | \psi \rangle \tag{2.16}$$

The term $F[n]$ is a density functional, that only depends on electronic properties, it is thus a functional that can also be expressed by the electron density as indicated by n. The kinetic energy of the electrons and their ground state wavefunction is unknown, as well as the external potential [7]. To circumvent this problem Kohn and Sham introduced a reformulated version of the problem. The many-body Schrödinger Equation is recast to a set of single particle equations. Here the Kohn-Sham potential [29], which contains all the unknown parameters of the system, is defined as follows:

$$v_{\mathrm{KS}}(\mathbf{r}, [n]) \; = \; v_{\mathrm{en}}(\mathbf{r}) + v_{\mathrm{H}}(\mathbf{r}) + v_{\mathrm{xc}}(\mathbf{r},\, [n]) \tag{2.17}$$

$v_{\mathrm{en}}(\mathbf{r})$ is the single particle electron-nucleon potential, $v_{\mathrm{H}}(\mathbf{r})$ is the Hartree-Potential, and $v_{\mathrm{xc}}(\mathbf{r},\, [n])$ is the single-particle exchange-correlation potential, defined by the following variation of the exchange-correlation energy due to the electronic density [30, 31]:

$$v_{\mathrm{xc}}(\mathbf{r},\, [n]) \; = \; \frac{dE_{\mathrm{xc}}[n]}{dn} \tag{2.18}$$

The Hartree potential accounts for the electron-electron interactions. It is defined as follows:

$$v_{\mathrm{H}} \; = \; \int d\mathbf{r}' \frac{n(\mathbf{r}')}{|\mathbf{r} - \mathbf{r}'|} \tag{2.19}$$

An indirect term that accounts for all the electron-electron interactions without scattering events is included in the exchange-correlation potential. Kohn and Sham showed, that the ground-state electron density of the interacting system coincides with the electron density of an auxiliary single-particle non-interacting system. With this the Kohn-Sham equation can be formulated, it is the single particle Schrödinger equation[]:

$$\left[-\frac{\Delta^2}{2} + v_{\mathrm{KS}}(\mathbf{r},[n]) \right] \phi_i^{\mathrm{KS}}(\mathbf{r}) \; = \; \varepsilon_i^{\mathrm{KS}}\, \phi_i^{\mathrm{KS}}(\mathbf{r}) \tag{2.20}$$

Here $\varepsilon_i^{\mathrm{KS}}$ and $\phi_i^{\mathrm{KS}}(\mathbf{r})$ are the single-particle Kohn-Sham energies and orbitals. The equation above is solved by iteration. The ground-state electron-density is defined as:

$$n_{\mathrm{GS}}(\mathbf{r}) = \sum_{i=1}^{\mathrm{N}} \left|\phi_i^{\mathrm{KS}}(\mathbf{r})\right|^2 \tag{2.21}$$

These equations form a set self consistent equations, with which it is possible to calculate the exact electron density of a system in the ground-state [7].
However, the exchange-correlation potential is unknown analytically and is therefore approximated. This can be done through Monte Carlo simulations and is an iterative process, described in the flowchart underneath.

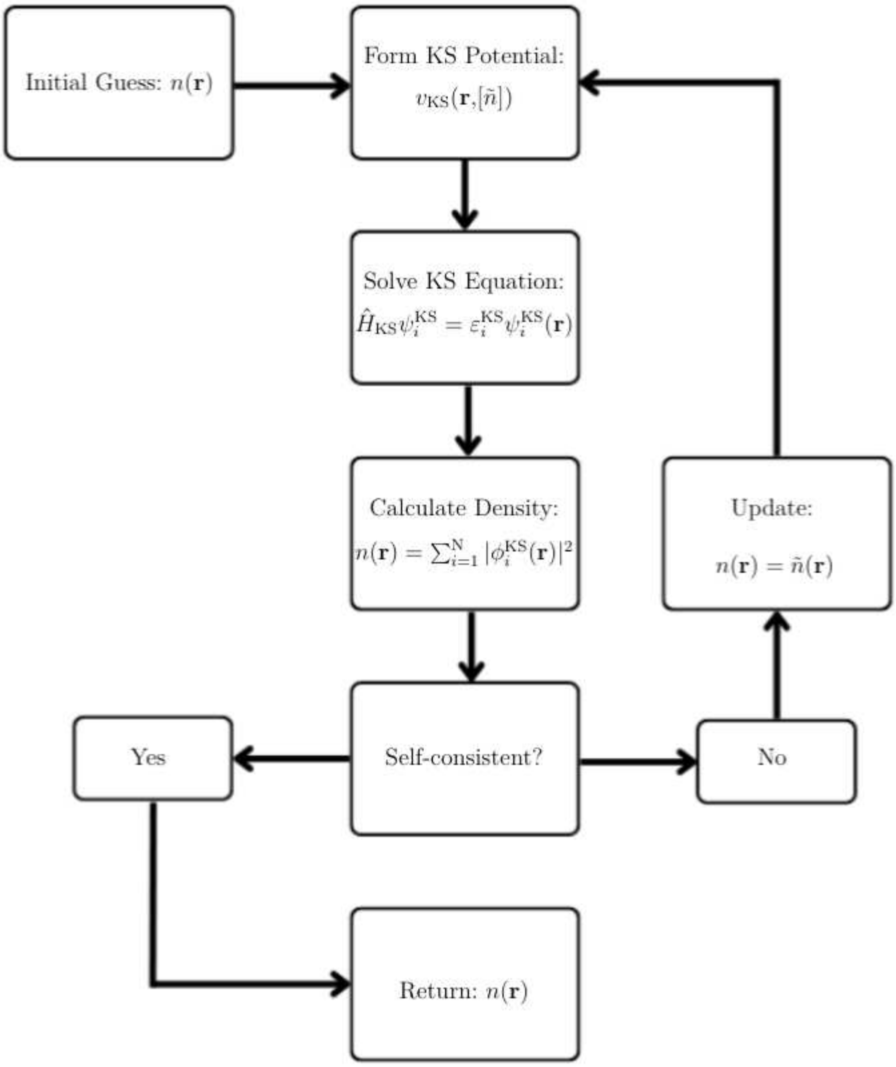

Figure 1: Flowchart of the approximation of the exchange-correlation potential.

The initial guess is usually defined as the electronic density at equilibrium. With this initial guess the Kohn-Sham potential is calculated and subsequently the Kohn-Sham equation is solved. With the solution a new density can be calculated, and if the outcome is self-consistent the current electronic density is returned. If this is not the case, the input for the electronic density is updated, the newly calculated density is now used in the same process until self consistency is reached. This is the case, if the initial guess, or the updated density is the same after an additional run through the procedure. Since a perfect match is connected to a long calculation time it is useful to set a value of convergence, that states the maximum variation allowed for the result to be considered self-consistent.

Using the aforementioned methods, systems with a number of electrons and nuclei approaching the Avogadro number can be considered. In the description of extended solids their periodicity can be used to further reduce the problem, in most cases to a single unit cell. This is done by taking into account the periodicity of the solid [32]. The Kohn-Sham potential in each unit cell is the same, resulting in the following description of the potential, using the lattice vector $\mathbf{R}$:

$$v_{\mathrm{KS}}(\mathbf{r}) \;=\; v_{\mathrm{KS}}(\mathbf{r}+\mathbf{R}) \tag{2.22}$$

The eigenfunctions solving the single-particle Schrödinger Equations are Bloch wavefunctions, defined in the following way:

$$\psi_{n,\mathbf{k}}(\mathbf{r}) \;=\; \frac{1}{\sqrt{N_p}} u_{n,\mathbf{k}}(\mathbf{r}) e^{i\mathbf{kr}} \tag{2.23}$$

Here n gives the band index, $\mathbf{k}$ is the momentum within the first Brillouin zone, N_p is the number of the unit cell and $u_{n,\mathbf{k}}(\mathbf{r})$ is a periodic function with the same periodicity as the crystal lattice. Considering only one primitive cell of the crystal is sufficient, when also using Born-von-Karman boundary conditions. Here a supercell is introduced, constructed of multiple unit cells and a reciprocal volume of the system given by the following expression, using the reciprocal volume of a single unit cell (Ω_p):

$$\Omega \;=\; N_p \Omega_p \tag{2.24}$$

The eigenfunction can be written as a Fourier series, with the reciprocal lattice vector $\mathbf{G}$ and the plane-wave coefficients $c_{n,\mathbf{k}}(\mathbf{G})$:

$$\psi_{n,\mathbf{k}}(\mathbf{r}) \;=\; \frac{1}{\sqrt{N_p \Omega_p}} \sum_{\mathbf{G}} c_{n,\mathbf{k}}(\mathbf{G})\, e^{i(\mathbf{k}+\mathbf{G})\cdot\mathbf{r}} \tag{2.25}$$

In the simulations the states are calculated for a finite number of $\mathbf{k}$-points given at the start, resulting in discrete eigenstates distributed over the unit cell. In the limit of an infinite number of $\mathbf{k}$-points these discrete values turn into a continuum, the eigenvalues $\varepsilon_{n,\mathbf{k}}$ turn into continuous bands. Computational limitations compel a truncation of the kinetic energies considered in the calculations. This value is defined as follows [33]:

$$\frac{|\mathbf{k}+\mathbf{G}|^2}{2} \leq E_{\text{cut}} \tag{2.26}$$

Due to this truncation convergence tests before the calculations are necessary, as any values of the kinetic energy above the cutoff will be neglected.
Another problem arises in the consideration of the core electrons. Their representation is not straightforward, as they are bound to the nucleus and therefore do not contribute to the chemical or physical properties of the material investigated. The core electrons can thus be described together with the nucleus, resulting in pseudopotentials [34, 35]. These describe the system with core electrons and the nucleus combined, considering the nuclear potential to be screened by the fixed core electrons. This makes the calculation of the structures less computationally expensive.

The pseudopotentials are transferable [35], as they can be used for atoms, molecules and bulk crystals alike. The goal is to describe the potential of the structure up to the ionic cutoff-radius correctly, behind which the pseudopotential coincides with the original potential and the pseudo-wavefunctions coincide with the original wavefunctions, as seen in the figure on the right. An important characteristic is the smoothness inside the ionic cutoff-radius, needed to obtain a good transition to the original potential. The logarithmic derivatives and the first energy derivatives of the wavefunctions must coincide for this goal to be completed. Pseudopotentials have been calculated for most atoms, with the norm conserving and ultrasoft pseudopotentials being the most common.

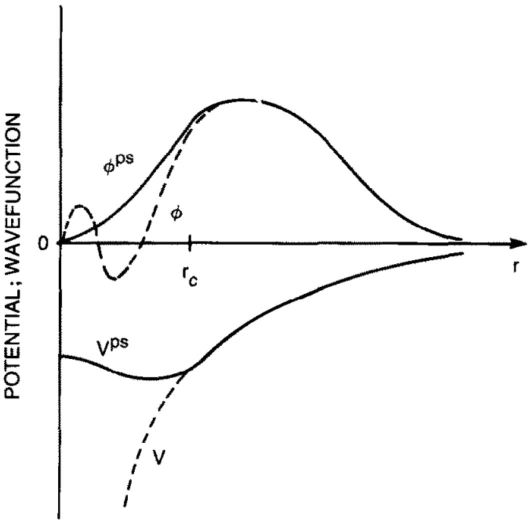

Figure 2: Schematic illustration of a Pseudopotential, taken from [36].

The former enforce two conditions. The first guarantees that the norm of the wavefunctions inside the cut-off radius are identical, the second guarantees that the wavefunctions are identical outside of the cutoff radius. The ultrasoft pseudopotentials relax the norm-conserving conditions and reduce the necessary basis-set size [37, 38]. The norm-conserving pseudopotentials were used in this work.
The Interaction between electrons and phonons, quasi-particles, that quantise the lattice vibrations, can be described via the Density Functional Perturbation Theory (DPFT) [7]. Here multiple electronic bands and phonon branches can be included. This theory goes beyond the equilibrium state of the system in DFT and introduces terms that drive the state

of the system out of equilibrium using perturbation potentials added to the Hamiltonian. For each possible interaction a new term is added. In the case of electronic and phononic systems the interactions between the phonons, the interactions between the electrons as well as the interaction between the phonons with the electrons and vice versa need to be considered. With these modifications and the solution of the Schrödinger Equation the system and its interactions can be described correctly.

2.2 Infrared Absorption

The transition between vibrational states involves inelastic scattering of light. The scattered light has a component which has a different frequency than the incident beam. The difference is exactly equal to the frequency of a phonon mode in the solid. This process is called Raman scattering for optical phonons and Brillouin scattering for acoustic phonons [39]. In optical experiments the intensity of the incident I_0, reflected I_R, transmitted I_T and absorbed I_A beams are measured. From energy conservation the following expression can be found:

$$I_0 = I_R + I_T + I_A \tag{2.27}$$

The apparent reflectivity, transmission and absorption can be found by dividing both sides by I_0:

$$\tilde{R} + \tilde{T} + \tilde{A} = 1 \tag{2.28}$$

The true values can only be found if the sample is sufficiently thick or in the ideal case, infinitely thick. The apparent absorption can be found by a measurement of the heating of the sample due to absorption of light, in some cases however measuring the thermal emission of the sample is more convenient. Optical properties like the reflectivity, or the absorption can be calculated using the complex dielectric function [40]. It can be defined as:

$$\varepsilon(\omega) = \varepsilon_1(\omega) + i\varepsilon_2(\omega) \tag{2.29}$$

In the case of optically isotropic materials. The complex refractive index is defined similarly: $\mathrm{n}(\omega) = \mathrm{n}_1(\omega) + i\mathrm{n}_2(\omega)$. Here n_1 is the refractive index and n_2 is the extinction coefficient. This leads to the following expression for ε_1 and ε_2:

$$\varepsilon_1 = \mathrm{n}_1^2 - \mathrm{n}_2^2 \tag{2.30}$$

$$\varepsilon_2 = 2 \cdot \mathrm{n}_1 \cdot \mathrm{n}_2 \tag{2.31}$$

The reflectivity an the absorption can now be expressed via the dielectric function ($\varepsilon(\omega)$), as follows:

$$\begin{aligned} R &= \frac{1-\sqrt{\varepsilon(\omega)}}{1+\sqrt{\varepsilon(\omega)}} && (2.32) \\ I(x) &= I_0 e^{-\alpha(\omega)x}, \text{ with} && (2.33) \\ \alpha(\omega) &= \frac{2\omega}{c}\mathrm{Im}(\sqrt{\varepsilon(\omega)}) && (2.34) \end{aligned}$$

The absorption of infrared light requires energy and momentum conservation. The energy of the photon ($\mathrm{E}_{\mathrm{phot}}$) needs to be equal to the energy of the phonon ($\mathrm{E}_{\mathrm{phon}}$), the photon momentum ($\mathbf{q}_{\mathrm{phot}}$) fixed by the dispersion relation $\omega = \mathrm{c}\mathbf{q}_{\mathrm{photon}}$, needs to be equal to the momentum of the phonon excited ($\mathbf{q}_{\mathrm{phon}}$). Additionally the values of $\mathbf{q}_{\mathrm{phon}}$ need to be compatible with the periodic boundary conditions, which leads to the following limitation in the case of a cubic unit cell with sidelength a: $-\frac{\pi}{a} < \mathbf{q} \leq \frac{\pi}{a}$. This puts the possible phonon frequencies for direct coupling of light to the phonon modes in the range of infrared light [1, 40].

The light-phonon interaction can be split up into two cases. For both an external electric field is applied in the form of $\mathbf{E} = \mathbf{E}\cos(\omega t)$. In the first case the unit cells consist of two or more atoms, with vanishing effective charges $\mathrm{Z}_1^* = \mathrm{Z}_2^* = \mathrm{Z}^* = 0$, as the electronic charge compensates the nucleon charge. In this case very weak to no coupling to the electromagnetic field can be observed [41, 29]. The effective charges are called Born Effective Charges (BEC). In the second case the BEC do not vanish. Due to sum rule the following relation needs to be obeyed: $\mathrm{Z}_1^* = -\mathrm{Z}_2^*$. The electromagnetic field couples to the effective nuclear charges. This case can be described by the Lorentz-Oscillator with the following motion equation: $\ddot{x} + \Omega_{\mathrm{TO}}^2 x = \frac{\mathrm{Z}_I^*}{\mu}\varepsilon(t)$, where μ stands for the mass, Z^* as before represents the effective charge and Ω_{TO} represents the phonon frequency of transverse optical phonons.

Infrared active phonons are the phonons in a system that absorb infrared light in a way that leads to a change of the polarisation in the system [41]. This does not apply to all phonon modes of the system however. In polar materials such as the one discussed in this work a unit cell is made up of multiple different atoms that do not have the same effective charge. As usual the effective charge in general is zero, $\sum_I \mathrm{Z}_I = 0$. In the long-wavelength limit only $\mathbf{q} = 0$ phonons can be absorbed, due to momentum conservation. The complex dielectric function, or rather the contribution of polar phonons to the optical response can be defined as follows:

$$\varepsilon_R = 1 + \frac{\sqrt{\varepsilon(\omega)}\mathrm{Z}_I^{*2}}{\varepsilon_0 \mu}\frac{1}{\Omega_{\mathrm{TO}}^2 - \omega^2} \tag{2.35}$$

The frequency that solves the equation $\varepsilon_R(\omega) = 0$ grants a total charge of zero, meaning that the following relation is also valid: $\mathbf{kE} = 0$. The electric field is transverse to the direction of propagation. The frequency of the transverse optical phonon modes are denoted as $\omega_{\mathrm{T=}}$, for a longitudinal field propagation the frequencies are denoted as ω_{LO}. The O denotes an optical phonon mode, as these are the modes that couple to the radiation, as the name suggests. For these frequencies a relation can be found, called Lyddane-Sachs-Teller Relation [29, 41]:

$$\frac{\varepsilon(\omega)}{\varepsilon_\infty} = \frac{\omega_{\mathrm{LO}}^2}{\Omega_{\mathrm{TO}}^2} \tag{2.36}$$

Through reflectivity experiments information on the LO-TO splitting can be extracted. This gives implications on infrared dielectric properties of polar semiconductors and insulators, which strongly reflect in the frequency region of $\omega_{\mathrm{TO}} < \omega < \omega_{\mathrm{LO}}$ [29]. This can be derived by evaluating the the response of a system to a time dependent driving electrical field. The dielectric function of the polar crystal exhibits a pole for $\omega = \omega_0 = \omega_{\mathrm{TO}}$ and equals 0 for ω_{LO}. Outside the interval between the LO and the TO frequencies the real part of the dielectric function is positive, while the imaginary part vanishes [40].
The real and imaginary part of the dielectric function can be expressed as a dispersion relation. These integrals relate an absorption process to a dispersion process. For $\varepsilon_1(\omega)$ and $\varepsilon_2(\omega)$ can be expressed as follows:

$$\varepsilon_1(\omega) = \frac{2}{\pi} P \int_0^\infty \frac{\omega' \varepsilon_2(\omega')}{\omega'^2 - \omega^2} d\omega' + 1 \tag{2.37}$$

$$\varepsilon_1(\omega) = -\frac{2\omega}{\pi} P \int_0^\infty \frac{\varepsilon_2(\omega') - 1}{\omega'^2 - \omega^2} d\omega' \tag{2.38}$$

Here P is the Cauchy Principle value. In consideration of interaction of lattice vibrations with infrared light the following Hamiltonian can be found:

$$H = H_0 + H' \text{ , where} \tag{2.39}$$

$$H_0 = H_{\mathrm{h}} + H_{\mathrm{anh}} \tag{2.40}$$

The Hamiltonian contains both a harmonic and an anharmonic as well as a harmonic contribution. H' stands for an external perturbation caused by interactions between the lattice and light. The perturbation is given by $H' = -\mathbf{E} \cdot \mathbf{M}$, $\mathbf{E}$ being the electric field of the light and $\mathbf{M}$ being the total dipole moment of the crystal. The electric field can be described as follows:

$$\mathbf{E} = \mathbf{E}_0 \exp[i \cdot (\mathbf{k} \cdot \mathbf{r} - \omega t)] \tag{2.41}$$

The wavelength λ is much larger in the infrared than the lattice parameter, since $k = \frac{2\pi}{\lambda}$, k is negligible. This means that $\mathbf{k} = 0$ and in first order processes the light-matter interaction involves only phonons with a wave vector $\mathbf{q} = \mathbf{0}$, which is at the Γ-point of the lattice.
In ionic crystals at $\mathbf{k} \approx 0$ the optical modes split into longitudinal (LO) and transversal (TO) optical branches. The TO branches are present due to the ions experiencing an additional restoring force arising from the charge polarisation. As a consequence the frequency of the LO branch has to be derived in different ways, since only the TO modes can participate in the absorption process. Here the Lyddane, Sachs and Teller relation is used [41, 29]:

$$\omega^2_{\mathrm{LO}}(\mathbf{k} \approx 0) \;=\; \frac{\varepsilon_s}{\varepsilon_\infty}\,\omega^2_{\mathrm{TO}}(\mathbf{k} \approx 0) \tag{2.42}$$

ε_s is the static dielectric constant and ε_∞ is the high frequency dielectric constant. In the two phonon absorption processes the two modes participating may have wave vectors different from zero. This in turn means that they do not transform according to representations of the space group G [39].
Under normal experimental circumstances only TO phonons can be excited in these processes [40], as follows from the definition of the perturbational Hamiltonian H', which it involves the scalar product of the electric field vector as well as the dipole moment of the crystal. The light is transversal, so the electric field vector ($\mathbf{E}$) is perpendicular to $\mathbf{k}$. For TO phonons the ionic displacement, and with it $\mathbf{M}$ is perpendicular to $\mathbf{q}$, which is parallel to $\mathbf{k}$, due to momentum conservation.
The dipole moment of the crystal can be expanded in a Taylor series with respect to ionic displacements [29, 42]:

$$\mathbf{M} \;=\; \mathbf{M}^{(0)} + \mathbf{M}^{(1)} + \mathbf{M}^{(2)} + ... \tag{2.43}$$

Here $\mathbf{M}^{(0)}$ is the static dipole moment of the crystal, which is usually equal to zero and is of no relevance for absorption. $\mathbf{M}^{(1)}$ however is linear in the ionic displacements and gives rise to one-phonon processes. $\mathbf{M}^{(2)}$ is quadratic in the displacements and leads to two-phonon absorption.
Both the absorption and the imaginary part of the dielectric constant depend on the matrix elements $\langle n'|\mathbf{M}|n\rangle$ for transitions from an initial state $\langle n|$ to a final state $|n'\rangle$. Calculating the eigenfunctions of the Hamiltonian shows, that the $\Phi^{(3)}$ mechanism and the $\mathbf{M}^{(2)}$ mechanisms, the two-phonon mechanisms, cannot be separated in ionic crystals due to cross-terms arising from the coupling of the two mechanisms. A discussion of the processes by neglecting one is possible by neglecting either $\mathbf{M}^{(2)}$, or H_{anh} [40].

Neglecting both $\mathbf{M}^{(2)}$ and H_{anh} leads to the discussion of the one-phonon-processes. In this approximation the Hamiltonian is defined as follows:

$$H = H_h - \mathbf{E} \cdot \mathbf{M}^{(1)} \tag{2.44}$$

A phonon is annihilated and a TO phonon with $\mathbf{q} \approx 0$ is created. In the phonon-photon conversion this process works in reverse, a phonon is annihilated and an induced photon is emitted. In the calculation of $\varepsilon(\omega)$ both these processes must be considered. Energy and momentum conservation requires:

$$\omega(\mathbf{k}) = \omega_{\text{TO}} \tag{2.45}$$

$$\mathbf{k} = \mathbf{q} \approx 0 \tag{2.46}$$

This approximation has its shortcomings. As an example it predicts an infinitely sharp absorption line at $\omega = \omega_{\text{TO}}$, when in experiments a rather broad line is found [40].
Two phonon processes due to the $\Phi^{(3)}$ mechanism are considered with a Hamiltonian approximated as follows:

$$H = H_0 - \mathbf{E} \cdot \mathbf{M}^{(0)} \tag{2.47}$$

This describes a mechanism in which a phonon can decay and experience a finite lifetime. The matrix elements $\langle n'|\mathbf{M}^{(1)}|n\rangle$ need to be solved by many-body techniques, as conventional perturbational techniques fail to describe these processes. The photon couples with an infrared TO phonon, the anharmonicity then couples the TO phonon with two other phonons, in summary three phonons are included in this process, with two phonons as an outcome. The mechanism conserves the overall energy, the momentum is conserved at each vertex, and the process satisfies the following conditions [40]:

$$\mathbf{k} = \mathbf{q} = \pm\mathbf{q}' \pm \mathbf{q}'' \approx 0 \tag{2.48}$$

$$\omega(\mathbf{k}) = \pm\omega_{j'}(\mathbf{q}') \pm \omega_{j''}(\mathbf{q}'') \tag{2.49}$$

Positive signs mean the creation of a phonon, negative signs mean the annihilation. Due to energy conservation the annihilation of two phonons is not possible, the creation of two phonons however is. In that case the vectors are of equal magnitude, but opposing signs. This is also the root of summation bands. Equally a creation of a phonon with $(\mathbf{q}', j')$ and another phonon with $(\mathbf{q}'', j'')$ is annihilated. This gives rise to difference bands. These processes can be summed up in the following equation:

$$\omega(\mathbf{k}) = \omega_{j'}(\mathbf{q}') \pm \omega_{j''}(\mathbf{q}'') \tag{2.50}$$

For summation bands the ($\pm$) is a plus, for difference bands it is a minus. The vectors are of equal magnitude, the branches may either be optical or acoustic. Anharmonic coupling between phonons is responsible for the broadening of the absorption line at $\omega = \omega_{\mathrm{TO}}$. The dampening depends both on the temperature and the frequency of the probing radiation [40].

This process can only be activated if a corresponding phonon is available. This phonon is an infrared active TO phonon, it induces a non-vanishing dipole Moment $\mathbf{M}^{(1)}$. This is however not the case for all crystals, as for example simple covalent crystals do not exhibit such behaviour.

Two-phonon processes can however also be triggered by the $\mathbf{M}^{(2)}$ mechanism, with the Hamiltonian:

$$H = H_h - \mathbf{E} \cdot \mathbf{M}^{(2)} \tag{2.51}$$

The matrix elements $\langle n' | \mathbf{M}^{(2)} | n \rangle$ are evaluated via the eigenfunction of the harmonic Hamiltonian. The products of two atomic displacements are contained in the second-order moment $\mathbf{M}^{(2)}$, therefore the $\mathbf{M}^{(2)}$-mechanism lets a photon couple to two phonons. The energy and momentum are conserved here as well.

The absorption of infrared radiation by a solid can be approached through the dipole approximation. In the presence of a vector potential $\mathbf{A}(\mathbf{r}, t)$ the kinetic energy of electrons and nucleons can be written as:

$$\hat{T}_e = \sum_i \left[\frac{\hat{\mathbf{p}}_i^2}{2m_e} + \frac{e}{m_e} \mathbf{A}(\mathbf{r}, t) \cdot \hat{\mathbf{p}}_i \right] \tag{2.52}$$

$$\hat{T}_n = \sum_{\kappa p} \left[\frac{\hat{\mathbf{P}}_{\kappa p}^2}{2M_\kappa} + \frac{Z_\kappa e}{M_\kappa} \mathbf{A}(\mathbf{r}, t) \cdot \hat{\mathbf{P}}_{\kappa p}^2 \right] \tag{2.53}$$

κ runs over the atoms in the unit cells, p runs over all cells in the Born-von-Karman supercell, i runs over the electrons in the system. Z_κ and M_κ denote the atomic number and nuclear mass of the κ-th nucleus. $\hat{\mathbf{P}}_{\kappa p}$ is the momentum operator of the κ-th nucleus in the p-th cell. $\hat{\mathbf{p}}_i$ is the electron momentum operator [40].

The vectorpotential in a classical monochromatic electromagnetic field, such as the one introducing the excitation in the system for this work, can be expressed by the following expression:

$$\mathbf{A}(\mathbf{r},t) = A_0 \pi \left[e^{i\mathbf{kr} - i\omega t} + e^{-i\mathbf{kr} + i\omega t} \right] \tag{2.54}$$

With π as the light polarisation vector, $\mathbf{k}$ and ω as the photon momentum and frequency respectively. The second term is responsible for stimulated emission, the first term is responsible for the absorption. At linear order the perturbation induced by the vectorpotential can be expressed as follows:

$$\hat{H}_{\text{int}} = \sum_i \frac{e}{m_e}\mathbf{A}\hat{\mathbf{p}}_i - \sum_{\kappa p}\frac{Z_\kappa e}{M_\kappa}\mathbf{A}\hat{\mathbf{P}}_{\kappa p} \tag{2.55}$$

The matrix elements of $\hat{H}_{\text{int}}$ give access to first-order perturbative corrections. The transitions between eigenstates are given by Fermi's Golden Rule:

$$\Gamma_{f\leftarrow i} = \frac{2\pi}{\hbar}\left|\langle\Psi_f|\hat{H}_{\text{int}}|\Psi_i\rangle\right|^2\delta(E_f - E_i - \hbar\omega) \tag{2.56}$$

Here the index i denotes the initial state and Energy of the system and f denotes the final state and Energy. $\hbar\omega$ is the photon energy and the transition matrix element can be decomposed into an electric and a nuclear part, both parts contribute to the absorption of infrared radiation:

$$\langle\Psi_f|\hat{H}_{int}|\Psi_i\rangle = \langle\Psi_f|\hat{H}^{\text{el}}_{int}|\Psi_i\rangle + \langle\Psi_f|\hat{H}^{\text{ph}}_{int}|\Psi_i\rangle \tag{2.57}$$

Using the Born Oppenheimer Approximation and focusing on the resonant absorption of infrared radiation in polar semiconductors the photon energy is smaller than the optical gap and no electronic transitions satisfy energy conservation. Thus the initial and final states coincide. In the following the matrix elements of the phononic term are evaluated.

Using $\Delta\hat{\tau}_{\kappa p}$, the derivation of the coordinate of the κ-th nucleus in the p-th cell from equilibrium due to lattice vibration the following expression is found [40]:

$$\langle\Psi_f|\hat{H}^{\text{ph}}_{\text{int}}|\Psi_i\rangle = -i\omega\sum_{\kappa p} Z_\kappa e\mathbf{A}\cdot\langle\chi_f|\Delta\hat{\tau}_{\kappa p}|\chi_i\rangle \tag{2.58}$$

Evaluating the last braket in this term and taking into account that the optical limit can be used due to the limitation to infrared radiation $\mathbf{k}$ is much smaller than the size of the Brillouin Zone, the following expression is valid:

$$\langle\Psi_f|\hat{H}^{\text{ph}}_{\text{int}}|\Psi_i\rangle = -ieA_0N_p^{\frac{1}{2}}(\hbar\omega)^{\frac{1}{2}}(n_\nu+1)^{\frac{1}{2}}e^{-i\omega t}\mathbf{F}^{\text{ph}}_\nu\cdot\pi \tag{2.59}$$

The following definition was used: $\mathbf{F}^{\text{ph}}_\nu = \sum_\kappa \frac{Z_\kappa e^\kappa_\nu}{\sqrt{2M_\kappa}}$. The electronic term can be rewritten using Fermi's Golden Rule, and $\hat{\mathbf{v}} = -\frac{i}{\hbar}[\hat{\mathbf{r}},\hat{H}]$. Leading to the following expression:

$$\langle\Psi_f|\hat{H}^{\text{el}}_{\text{int}}|\Psi_i\rangle = i\sum_j e\omega\mathbf{A}\cdot\langle\Psi_f|\hat{\mathbf{r}}_j|\Psi_i\rangle \tag{2.60}$$

Now $\langle \Psi_f | \hat{\mathbf{r}}_j | \Psi_i \rangle$ needs to be evaluated:

$$\sum_j \langle \Psi_f | \hat{\mathbf{r}}_j | \Psi_i \rangle \; = \; \sum_{\kappa p} \langle \chi_f | \Delta \tau_{\kappa p} | \chi_i \rangle \cdot \mathbf{Z}^{*,\mathrm{el}}_{\kappa} \tag{2.61}$$

With the last term ($\mathbf{Z}^{*,\mathrm{el}}_{\kappa}$) being the Born-Effective-Charge tensor, defined as:

$$\mathbf{Z}^{*,\mathrm{el}}_{\kappa,\alpha\beta} \; = \; \frac{\hbar}{N_p} \sum_{n\mathbf{k}}^{\mathrm{occ.}} 2\mathrm{Im}\, \langle \partial_{\kappa p \alpha} u_{n\mathbf{k}} | \hat{T}_{n\mathbf{k}\hat{v}_{\mathbf{k}}} | u_{n\mathbf{k}} \rangle \tag{2.62}$$

This is identical in all cells, since $u_{n\mathbf{k}}$ is cell periodic. The final expression for the electronic term can be given as:

$$\langle \Psi_f | \hat{H}^{\mathrm{el}}_{\mathrm{int}} | \Psi_i \rangle \; = \; i N_p^{\frac{1}{2}} e A_0 (\hbar\omega)^{\frac{1}{2}} (n_\omega + 1)^{\frac{1}{2}} e^{-i\omega t} \mathbf{F}^{\mathrm{el}}_{\nu} \cdot \pi \tag{2.63}$$

With Fermi's Golden Rule the following expression for the rate of phonon emission per unit cell, the scattering rate, which is of interest in this work, can be defined as follows [43]:

$$\Gamma_\nu \; = \; \frac{2\pi}{\hbar} (eA_0)^2 |\mathbf{F}_\nu \cdot \pi|^2 (n_\nu + 1) \hbar\omega_\nu \delta(\hbar\omega - \hbar\omega_\nu) \tag{2.64}$$

With this quantity the scattering of phonons excited by infrared radiation into other phonon modes can be traced. Thus the preferred thermalisation paths can be determined.

2.3 Time-Dependent Boltzmann Equation

The interactions of electrons and phonons is one of the fundamental interaction mechanisms in solids [30]. A variety of properties of the solids are determined or affected by it, such as the band effective mass, the fundamental gap or the charge transport. Phonon assisted scattering processes further hold an important role in ultrafast dynamics of electrons and phonons and determine the thermalization timescale [24].

The Time-Dependent Boltzmann Equation (TDBE) provides an approach to a description of electron-phonon coupling and its influence on dynamics 33. The Boltzmann Transport Equation (BTE) is the underlying theoretical approach of the first-principles work in carrier and phonon dynamics. It describes the dynamics in phase-space and through electron and phonon occupations. This is a semi-classical approach since both the crystal position and momentum are specified at the same time [7].

The dynamics described by the BTE are split into two parts. One is a slowly varying flow, induced by external fields called drift. This will not be of any particular interest in this work. The other part includes collision dynamics of electrons and phonons. The BTE is adequate to describe a timescale of multiple scattering events.

With the TDBE the phase-space constraints in the phonon-assisted scattering processes and the anisotropies of the electron-phonon coupling are accounted for. The TDBE was successfully applied to a variety of problems in two and three dimensions for semiconductors and metals, as well as in the investigation of ultrafast magnetisation dynamics in photo-excited ferromagnets [24, 44, 8]. One of the advantages over other, simplified models is the ability to investigate coupled non-equilibrium dynamics of electrons and phonon populations while having full momentum resolution, which allows the investigation of the anisotropic population of the electronic and vibrational states in reciprocal space.

The TDBE is a compromise between accuracy and efficiency, without neglecting either. The properties used to describe the dynamics in the crystal are the electronic and phonon distribution functions $n_{\mathbf{q}\nu}(t)$ and $f_{n\mathbf{k}}(t)$, without a change in the energies for either of the systems. At equilibrium the distribution functions are equal to the Fermi-Dirac and the Bose-Einstein distribution:

$$f^0_{n\mathbf{k}}(t) = \left[e^{(\varepsilon_{n\mathbf{k}}-\varepsilon_F)/k_BT}+1\right]^{-1} \tag{2.65}$$

$$n^0_{\mathbf{q}\nu}(t) = \left[e^{\hbar\omega_{\mathbf{q}\nu}/k_BT}-1\right]^{-1} \tag{2.66}$$

ε_F is the Fermi energy, $\varepsilon_{n\mathbf{k}}$ is the single particle energy of a Bloch electron and $\hbar\omega_{\mathbf{q}\nu}$ is the phonon energy. In a non-equilibrium state either $n_{\mathbf{q}\nu}(t)$, $f_{n\mathbf{k}}(t)$, or both differ from the equilibrium state and change over time:

$$\partial_t f_{n\mathbf{k}}(t) = \Gamma_{n\mathbf{k}}(t) \tag{2.67}$$

$$\partial_t n_{\mathbf{q}\nu}(t) = \Gamma_{\mathbf{q}\nu}(t) \tag{2.68}$$

$\Gamma_{n\mathbf{k}}$ and $\Gamma_{\mathbf{q}\nu}$ are the collision integrals for the electrons and the phonons respectively. These account for the scattering mechanisms which may lead to changes of the distributions. These mechanisms can be scattering among the electrons and the phonons among themselves as well as with each other, impurity scattering is also possible, as is coupling to external fields. With the development in the electronic structure codes the calculation of these processes is possible, enabling the investigation of coupled dynamics from first principles [7].

The derivation of the expressions for the electron-phonon and phonon-phonon collision integrals are built upon Fermi's golden rule. It is used to calculate rates and timescales of electron-phonon scattering processes. The scattering is described by matrices containing elements of the perturbation potential and the phase space of available states [1]:

$$\Gamma_{\alpha_i} = \frac{2\pi}{\hbar}\sum_{\alpha_f}\left|M_{\alpha_i,\alpha_f}\right|^2\delta(E_{\alpha_i}-E_{\alpha_f}) \tag{2.69}$$

Here Γ_{α_i} is the scattering rate. Considering the initial state α_i after a scattering process the final state α_f is found. The Hamiltonian in a system with electron-phonon and phonon-phonon interactions can be written as:

$$\hat{H} \;=\; \hat{H}_e + \hat{H}_p + \hat{H}_{ep} + \hat{H}_{pp} \tag{2.70}$$

$\hat{H}_e$ is the electronic Hamiltonian, $\hat{H}_p$ describes the Hamiltonian of the lattice in the harmonic approximation. $|\chi_s\rangle = \Pi_{\mathbf{q}\nu}\, |n\rangle^s_{\mathbf{q}\nu}$ are the eigenstates of $\hat{H}_p$. Here $|n\rangle^s_{\mathbf{q}\nu}$ are the eigenstates of the number operator with eigenvalue $n^s_{\mathbf{q}\nu}$, which in turn is the occupation number of the bosonic mode. ν and $\mathbf{q}$ denote the quantum numbers and s denotes the number of the eigenstate. The energy of the harmonic lattice can be expressed as follows [7, 29]:

$$\hat{H}_{pp} \;=\; \frac{1}{3!}\sum_{\mathbf{q}\mathbf{q}'\mathbf{q}''}\sum_{\nu\nu'\nu''}\Psi_{\substack{\mathbf{q}\mathbf{q}'\mathbf{q}''\\ \nu\nu'\nu''}}[\hat{a}_{\mathbf{q}\nu}+\hat{a}^\dagger_{-\mathbf{q}\nu}][\hat{a}_{\mathbf{q}\nu}+\hat{a}^\dagger_{-\mathbf{q}'\nu'}][\hat{a}_{\mathbf{q}''\nu''}+\hat{a}^\dagger_{-\mathbf{q}''\nu''}] \tag{2.71}$$

In this equation Ψ denotes the phonon-phonon scattering matrix related to the three phonon scattering process probability amplitude. To derive the collision integrals the weak nature of the electron-phonon and the phonon-phonon interactions in solids are considered. Thus the corresponding terms in the Hamiltonian can be treated as perturbations. Via Fermi's golden rule the transition rate from initial state $|i\rangle$ to final state $|f\rangle$ can be obtained:

$$\Gamma_{i\to f} \;=\; \frac{2\pi}{\hbar}|\,\langle f|\hat{V}|i\rangle\,|^2\delta(E^{\mathrm{tot}}_f - E^{\mathrm{tot}}_i) \tag{2.72}$$

Here $\hat{V}$ is an arbitrary perturbation. The initial and final state are formulated in a Born-Oppenheimer Ansatz:

$$|i\rangle \;=\; |\Psi_i\rangle\,|\chi_i\rangle \tag{2.73}$$

$|\Psi_i\rangle$ and $|\chi_i\rangle$ are the eigenstates of the harmonic Hamiltonian and the electronic Hamiltonian respectively. The following is an expression of the matrix elements of the electron-phonon coupling Hamiltonian [7]:

$$\langle f|\hat{H}_{\mathrm{ep}}|i\rangle \;=\; N_p^{-\frac{1}{2}}\sum_{nm\nu}\sum_{\mathbf{k}\mathbf{q}} g^{\nu}_{nm}(\mathbf{k},\mathbf{q})\,\langle\Psi_f|\hat{c}^\dagger_{m\mathbf{k}+\mathbf{q}}\hat{c}_{n\mathbf{q}}|\Psi_i\rangle\,\langle\chi_i|\hat{a}_{\mathbf{q}\nu}+\hat{a}^\dagger_{a\mathbf{q}\nu}|\chi_i\rangle \tag{2.74}$$

The matrix elements of the fermionic operator yield a value different from zero if $|\Psi_i\rangle$ and $|Psi_f\rangle$ differ only in the occupation of the $n\mathbf{q}$ and $m\mathbf{q}+\mathbf{k}$ states. If that is the case the following correlation applies:

$$\langle\Psi_f|\hat{c}^\dagger_{m\mathbf{k}+\mathbf{q}}\hat{c}_{n\mathbf{k}}|\Psi_i\rangle \;=\; \Big[f_{n\mathbf{k}}(1-f_{m\mathbf{k}+\mathbf{q}})\Big]^{\frac{1}{2}} \tag{2.75}$$

A similar correlation can be found in the case of the bosonic operators and the vibrational states. The total absorption rate of a phonon with the quantum numbers $\mathbf{q}\nu$ can be written as follows:

$$\Gamma^{\mathrm{abs}}_{\mathbf{q}\nu} = \frac{4\pi}{\hbar N_p} \sum_{mn\mathbf{k}} |g^{\nu}_{mn}(\mathbf{k},\mathbf{q})|^2 \, f_{n\mathbf{k}}(1 - f_{m\mathbf{k}+\mathbf{q}}) \, \delta(\varepsilon_{n\mathbf{k}} + \hbar\omega_{\mathbf{q}\nu} - \varepsilon_{m\mathbf{k}+\mathbf{q}}) n_{\mathbf{q}\nu} \tag{2.76}$$

The expression in the δ function denotes the total energy difference between the initial and final state. Using the same procedure and considering phonon emission processes yields [39]:

$$\Gamma^{\mathrm{em}}_{\mathbf{q}\nu} = \frac{4\pi}{\hbar N_p} \sum_{mn\mathbf{k}} |g^{\nu}_{mn}(\mathbf{k},\mathbf{q})|^2 \, f_{n\mathbf{k}}(1 - f_{m\mathbf{k}+\mathbf{q}}) \, \delta(\varepsilon_{n\mathbf{k}} - \hbar\omega_{\mathbf{q}\nu} - \varepsilon_{m\mathbf{k}+\mathbf{q}})(n_{\mathbf{q}\nu} + 1) \tag{2.77}$$

The total rate of change in phonon occupation due to electron-phonon processes can be defined as the difference between the aforementioned processes:

$$\begin{aligned} \Gamma^{\mathrm{pe}}_{\mathbf{q}\nu} = {} & \frac{4\pi}{\hbar N_p} \sum_{mn\mathbf{k}} |g^{\nu}_{mn}(\mathbf{k},\mathbf{q})|^2 \, f_{n\mathbf{k}}(1 - f_{m\mathbf{k}+\mathbf{q}}) \\ & \times [\delta(\varepsilon_{n\mathbf{k}} - \hbar\omega_{\mathbf{q}\nu} - \varepsilon_{m\mathbf{k}+\mathbf{q}})(n_{\mathbf{q}\nu} + 1) - \delta(\varepsilon_{n\mathbf{k}} + \hbar\omega_{\mathbf{q}\nu} - \varepsilon_{m\mathbf{k}+\mathbf{q}}) n_{\mathbf{q}\nu} \end{aligned} \tag{2.78}$$

The time dependence in the expression above arises from the changes in both the electron and the phonon distribution functions. In the case of thermal equilibrium the occupation relations are equal to the Fermi-Dirac and the Bose-Einstein distribution functions for the electrons and the phonons respectively [1].

With similar steps the electronic collision integral due to the electron-phonon interaction can be found in the following form:

$$\begin{aligned} \Gamma^{\mathrm{ep}}_{n\mathbf{k}}(t) = {} & \frac{4\pi}{\hbar N_p} \sum_{m\nu\mathbf{k}} |g^{\nu}_{mn}(\mathbf{k},\mathbf{q})|^2 \\ & \times \Big[(1 - f_{n\mathbf{k}}) f_{m\mathbf{k}+\mathbf{q}} \delta(\varepsilon_{n\mathbf{k}} - \varepsilon_{m\mathbf{k}+\mathbf{q}} + \hbar\omega_{\mathbf{q}\nu})(1 + n_{\mathbf{q}\nu}) \\ & + (1 - f_{n\mathbf{k}}) f_{m\mathbf{k}+\mathbf{q}} \delta(\varepsilon_{n\mathbf{k}} - \varepsilon_{m\mathbf{k}+\mathbf{q}} - \hbar\omega_{\mathbf{q}\nu}) n_{\mathbf{q}\nu} \\ & - f_{n\mathbf{k}}(1 - f_{m\mathbf{k}+\mathbf{q}}) \delta(\varepsilon_{n\mathbf{k}} - \varepsilon_{m\mathbf{k}+\mathbf{q}} - \hbar\omega_{\mathbf{q}\nu})(1 + n_{\mathbf{q}\nu}) \\ & - f_{n\mathbf{k}} (1 - f_{m\mathbf{k}+\mathbf{q}}) \delta(\varepsilon_{n\mathbf{k}} - \varepsilon_{m\mathbf{k}+\mathbf{q}} + \hbar\omega_{\mathbf{q}\nu}) n_{\mathbf{q}\nu}\Big] \end{aligned} \tag{2.79}$$

The first two parts of this equation denote the scattering of an electron from $m\mathbf{k}+\mathbf{q}$ to $n\mathbf{k}$ via the emission or absorption of a phonon while the latter two parts represent the scattering from $n\mathbf{h}$ to $m\mathbf{k} + \mathbf{q}$ due to phonon emission or absorption. If a thermal equilibrium is established in the system $\Gamma^{\mathrm{ep}}_{n\mathbf{k}} = 0$. Deriving the scattering rate due to phonon-phonon processes involves the evaluation of matrix elements of bosonic operators resulting in the following expression:

$$\begin{aligned}\Gamma^{\mathrm{pp}}_{\mathbf{q}\nu}(t) &= \frac{2\pi}{\hbar}\sum_{\nu'\nu''}\int\frac{d\mathbf{q}'}{\Omega_{\mathrm{BZ}}}\left|\Psi^{\nu\nu'\nu''}_{\mathbf{q}\mathbf{q}'\mathbf{q}''}\right|^2 \\ &\times [[\,(n_{\mathbf{q}\nu}+1)(n_{\mathbf{q}'\nu'}+1)n_{\mathbf{q}''\nu''} - n_{\mathbf{q}\nu}n_{\mathbf{q}'\nu'}(n_{\mathbf{q}''\nu''}+1)]\delta(\omega_{\mathbf{q}\nu}+\omega_{\mathbf{q}'\nu'}-\omega_{\mathbf{q}''\nu''})\delta^{\mathbf{G}}_{\mathbf{q}\mathbf{q}'-\mathbf{q}''} \\ &+ \frac{1}{2}[\,(n_{\mathbf{q}\nu}+1)n_{\mathbf{q}'\nu'}n_{\mathbf{q}''\nu''} - n_{\mathbf{q}\nu}(n_{\mathbf{q}'\nu'}+1)(n_{\mathbf{q}''\nu''}+1)]\delta(\omega_{\mathbf{q}\nu}-\omega_{\mathbf{q}'\nu'}-\omega_{\mathbf{q}''\nu''})\delta^{\mathbf{G}}_{\mathbf{q}-\mathbf{q}'-\mathbf{q}''}]\end{aligned} \tag{2.80}$$

Here the Kronecker Delta equals unity if $\mathbf{q} = 0$ or $\mathbf{q} = \mathbf{G}$. $\mathbf{G}$ denotes a reciprocal lattice-vector. If neither is the case the delta function equals 0. With these expressions the Boltzmann equation can be rewritten using the collision integrals:

$$\partial_t f_{n\mathbf{k}}(t) = \Gamma^{\mathrm{ep}}_{n\mathbf{k}}[f_{n\mathbf{k}}(t), n_{\mathbf{q}\nu(t)}] \tag{2.81}$$

$$\partial_t n_{\mathbf{q}\nu}(t) = \Gamma^{\mathrm{pe}}_{\mathbf{q}\nu}[f_{n\mathbf{k}}(t), n_{\mathbf{q}\nu(t)}] + \Gamma^{\mathrm{pp}}_{\mathbf{q}\nu}[n_{\mathbf{q}\nu}(t)] \tag{2.82}$$

Finding a solution to the last two equations requires a definition of an initial excited state characterised by the occupation function differing from equilibrium, either the electronic, or the phononic occupations. In the next step a solution to the differential equation needs to be found. This is an iterative process, the collision integrals are updated at each time step. Phonon emission processes are constrained by energy and momentum conservation laws which reduce the phase-space available for the phonon assisted electronic transitions. In the case of graphene carriers in the vicinity of the Fermi level at $\mathbf{K}$ can scatter within the same Dirac cone with $\mathbf{q} \approx \Gamma$, or to the second Dirac cone at $-\mathbf{K}$, emitting phonons with crystal momentum around $\mathbf{K}$, or $-\mathbf{K}$. This results in the emergence of hot spots in the BZ. These regions are defined by higher vibrational temperatures.

Without driving external fields solving the coupled Boltzmann Transport Equations involves a large number of differential equations, making the calculation computationally expensive. The number of differential equations equates to $N_b \times N_k \times N_\nu \times N_{\mathbf{q}}$. N_b is the number of bands, N_k is the number of k-points, N_ν is the number of phonon branches and $N_{\mathbf{q}}$ is the number of $\mathbf{q}$-points [5].

3 Methods

The codes and structures, as well as the parameters used in this work are of special interest. Starting with the codes that are used to calculate the structure, Quantum Espresso is used for the setup of the structure, with ShengBTE calculating the thermalisation of a lattice excited by infrared light. This excitation is exemplified by a depiction of the population increase due to infrared absorption. The lattice, or more precisely the crystal examined in this work and the relaxation and thermalisation of the grid will also be discussed here.

3.1 Transition Metal Dichalcogenide Monolayers

Transition Metal Dichalcogenide Monolayers (TMDs) are a group of atomically thin semiconductors. They are of the type MX_2, where M is a transition metal such as Molybdenum (Mo), or Tungsten (W) and X is a chalcogen atom such as Selenium (Se) or Sulphur (S). 44 TMD compounds can form stable two-dimensional structures exhibiting polymorphism, a unique feature of TMDs in bulk configuration [45]. The layered structure consists of two chalcogen layers enveloping a layer of the transition metal. Although the TMDs are technically not two-dimensional, they belong to the group of so-called 2D materials due to their thinness. A monolayer MoS_2 has a thickness of 6.5Å for example. This group of semiconductors exhibits superconductivity [46] and are the subject of a lot of research surrounding for example renewable energies [11].

The materials can be found in the pseudo two dimensional configuration, as well as in a bulk. The bulk consists of a number of layers of the monolayer. These are bound to each other with by van-der-Waals interaction. In comparison with graphene, a material that has opened the door for new experiments with monolayers showing different properties than the bulk crystal, a number of differences can be spotted. One of which is a tunable direct band gap, which means that the TMDs can be used in electronics as transistors [10]. The absence of an inversion centre in the case of a monolayer (or an uneven number of layers) means that the crystal is subject to valleytronics [47], a rather new field of physics. The hexagonal lattice has threefold symmetry and due to its layered structure it forms nanotubes, which are subject to research and a promising topic in the context of energy storage. It is currently used in catalysts, lasers, lubricants or photodetectors as well as batteries [13, 14].

For the bulk material 18 phonon modes are available, which is cut down to 9 in a monolayer. Although present, the frequency splitting between the monolayer and the bulk material is rather small, due to the layer interaction via van der Walls forces [48].

In this work Tungsten Disulfide (WS_2) will be investigated, more specifically a monolayer. Like other TMDs, WS_2 has a hexagonal, honeycomb structure. It can occur naturally as the mineral tungstenite, although it is rather rare. In experiments WS_2 is synthesised via chemical vapour deposition, physical vapour deposition or other methods [49]. In the configuration of an atomically thin sheet photo-luminescence can be observed [45]. In Fig. 3 the unit cell that is used in this work can be found. The crystallisation is realised in the hexagonal P6$_3$/mmc space group. The two WS_2 sheets are oriented in the (0,0,1) direction. The W^{4+} atom is bonded to two S^{2-} atoms forming distorted edge-sharing WS_6 pentagonal pyramids.

In the case of a monolayer WS_2 indirect-to-direct bandgap transitions will occur due to the stability of the valence band state of Γ. The direct band gap at the K-point however does not change with the thickness of the crystal, due to the valence and conduction band states at K not being affected by interlayer interactions.

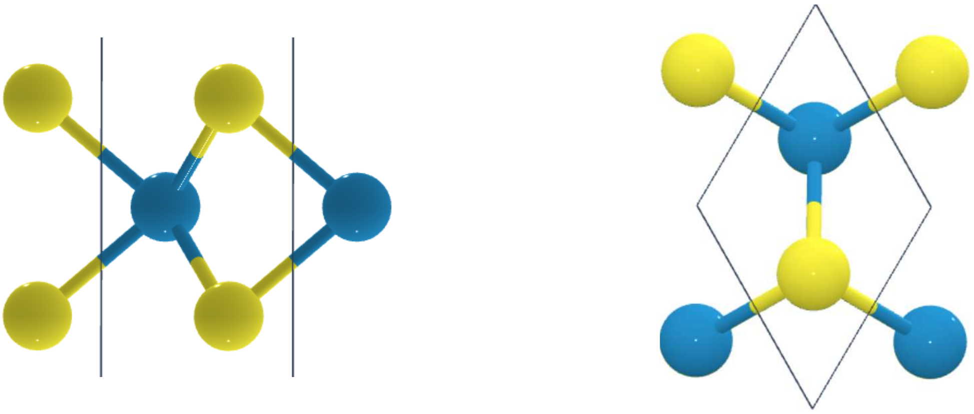

Figure 3: Side- and top-view of the structure of WS_2 in the two-dimensional form. Data retrieved from the Materials Project for WS2 (mp-224) from database version v2021.11.10. The Sulphur atoms depicted in yellow, Tungsten atoms depicted in blue.

A wide variety of applications for WS_2 can be found [45]. Layered WS_2 for example can be used as photocatalyst in the production of clean energy, especially in photovoltaic systems. The electrocatalyst properties on the other hand facilitate hydrogen evolution reactions. Additionally in recent research a use in fibre, and solid-state laser saturable absorbers is found, as the tunabale bandgap is useful. These properties of WS_2 make it a useful option to replace graphene, as the graphene nanotubes show less beneficial saturation absorption characteristics. Other uses include lithium-ion batteries, photodetectors, lubricants for mechanical manufacturing, gas sensors and field-effect transistors.

3.2 Quantum Espresso

Quantum Espresso (QE) is an open-source suite of computer codes for electronic-structure calculations and materials modelling. Its basis is the Density Functional Theory (DFT), plane waves, and pseudopotentials. The codes included are capable of performing a variety of tasks. The WANNIER90 package for example is used in the calculation of maximally localised Wannier functions. QE also plays a key role in the setup of the calculations done in this work as some of the outputs of the QE calculations are inputs to the ShengBTE code.

Specifically the setup of the grid is done here.
In order to achieve optimal inputs a couple of steps in the QE calculation are needed. First the crystal needs to be defined via the materialsproject, a website from which the input data for QE can be obtained. This will be used to perform the calculations with QE.
In the first step the crystal structure and the unit cell will be relaxed. The goal of this calculation is to bring the forces acting inside the crystal to a minimum, ideally to zero. In QE simulations that involve phonons it is common that imaginary phonon frequencies arise in the calculations, this is nonphysical and thus needs to be avoided. The next step is to perform a self consistent field calculation with the relaxed atomic positions. The scf calculation solves the Kohn-Sham equation of the crystal self-consistently. As the third step a calculation of the phonons in the crystal is done for a single **q**-point, which in this case is the Γ-point, where the phonon momentum $\mathbf{q} = 0$. The calculations of the interatomic force constants are passed on to calculate input files for ShengBTE, which will be addressed later.

3.3 The scattering rate for IR Absorption

The calculation of the scattering rate for infrared absorption is done through post-processing of the output data of the QE calculations. First the atomic masses and the Born Effective Charges (BEC) are taken from the output. The BEC (Z^*_κ) are the charges that occur due to the interaction of the tungsten and sulphur atoms in the material, when the atoms move relative to each other. This is vital in the consideration of infrared absorption, as only the infrared active modes contribute to the absorption process. These modes are the only ones with a non-vanishing dipole. The BEC are defined as follows:

$$Z^*_\kappa = \frac{\partial \mathbf{P}}{\partial \Delta \tau_{\kappa p}} \tag{3.1}$$

Here **P** is the electric dipole momentum and $\Delta_{\kappa p}$ is the displacement of the charges. The first step in the calculation of the impact of the infrared absorption is the calculation of $\mathbf{F}_\nu$, an intermediate quantity, defined as: $\mathbf{F}_\nu = \sum_\kappa \frac{\mathbf{e}_\kappa \cdot \mathbf{Z}^*_\kappa}{\sqrt{w M_\kappa}}$. This quantity is only non-zero if the respective phonon mode, denoted by the ν in the index, is infrared active, as it includes the BEC. The vector $\mathbf{e}_\kappa$ stores the phonon eigenvectors. This allows for an evaluation of the scattering rate. The collision integral from Fermi's Golden Rule is given by:

$$\Gamma_\nu = \frac{2\pi}{\hbar}(eA_0)^2 |\mathbf{F}_\nu \cdot \pi|^2 (n_\nu + 1)\delta\Big(1 - \frac{\omega_\nu}{\omega}\Big) \tag{3.2}$$

Here π is the light polarisation vector, $(e\,A_0)^2$ is the field intensity of the electromagnetic radiation, n_ν describes the phonon population in the mode ν and ω_ν describes the corresponding phonon frequency. With this property the rate of the increase of phonon population in a solid due to infrared light is described. This is implemented without the field intensity

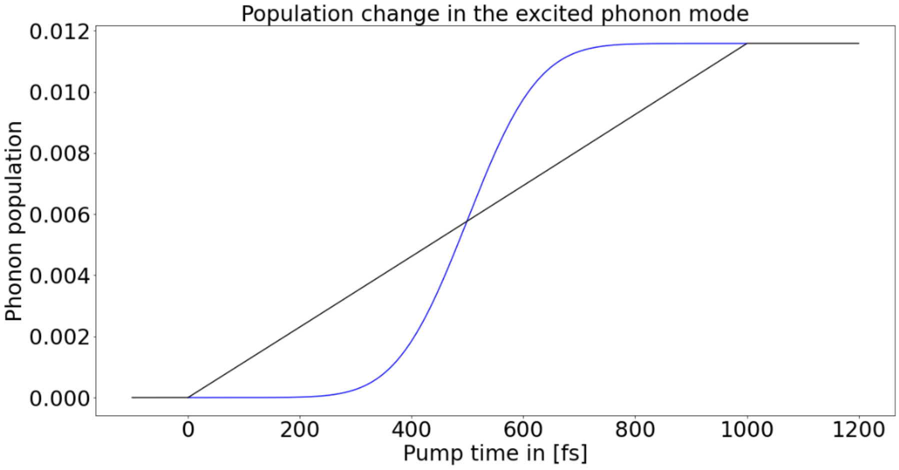

Figure 4: Effect of the IR pump on the phonon population with a pump duration of $1ps$. The reflected field intensity is at 60% with the transmitted field intensity at 20% and fluence of 55[mJ/cm^2]. The time-integrated absorbed fluence is 11 [mJ/cm^2]. In black the pump has the form of a Heaviside function, in the blue graph a realistic pump in form of a gaussian function is calculated.

and without the delta-function $\delta(1-\frac{\omega_\nu}{\omega})$. The field intensity is included by other means and can be changed if needed.

After this consideration an evaluation of the effect of the pump process after a certain time on the phonon population in the material is needed. First the grid for the time propagation has to be set. This is done by setting a starting time, which in this case is −100fs, an ending time, 1200fs in this case, as well as a length for the steps in time (0.01fs). The overall duration of the pulse in the example below is set to 1300fs with a pulse duration of 1000fs. Subsequently the time propagation is performed. With every step in time the phonon population is updated. A reflectivity of 0.6 and a transmission of 0.2 is assumed. In Fig. 4 the effect of the IR pump on the phonon population in WS_2 can be seen. An increase of the phonon population of the phonon mode that is active in this case is observed in the time the IR pump is active. After the electromagnetic radiation is cut off no further increase is seen. In this figure after the end of the pump process the population is constant. In a real system this would not be the case, as the population of the excited phonon mode would decrease and scatter into other modes. The horizontal line after the pump process is used to clarify, that the population does not increase without a the infrared radiation.

In general the transverse optical phonon modes couple strongly to infrared radiation, as the radiation waves are transverse as well. The LO phonon modes however also play an important role in the infrared properties of crystals [41]. The energy of the grid is calculated. The energy gained by the lattice is 0.002[eV] and the total energy of the pulse is 189.7[eV].

3.4 ShengBTE

ShengBTE is the code used for the time evolution of the system. As the name suggests it evaluates the Boltzmann Transport Equation for Phonons, from an equilibrium state. The code relies on the output files of Quantum Espresso, namely the second and third order force constants. The third order force constant (3FC) is obtained via the thirdorder_espresso.py code, a script available with the ShengBTE code.

In the CONTROL file the system to be studied is described by a set of flags and crystal parameters. This file is filled by the user. New parameters can be introduced, as ShengBTE allows the user to alter the code, as well as the calculation itself. This has been done in this case, to suit the requirements of the planned simulation.

In this work the code is altered in order to enable the calculation to run as wished. Most importantly a possibility is introduced to excite one phonon mode at a specific point in the Brillouin Zone, like the Γ-point. The temperature as well as the grid density of the current calculation, the broadening parameter, the number of time steps and their length can be set manually.

Another change in the code is needed to guarantee comparability between different grid densities. In the original version of the code the different densities were not comparable, due to the energy of the crystal varying with different grid densities, which is to be avoided. The reason behind this is, that by setting a grid density the simulated cell is divided up in as many parts. As an example, a $200 \times 200 \times 1$ grid divides the cell into 40000 parts, a $40 \times 40 \times 1$ grid yields 1600 parts. By increasing the temperature of the phonon mode at the Γ-point only one of these parts is heated. The denser the grid, the smaller the area heated. The energy of the lattice is thus different for every density. By setting a default value for the grid density and rescaling the number of phonons excited this issue is solved. In the ShengBTE calculation the following expression gives the number of excited phonons in the excited mode:

$$\tilde{n}_{\mathbf{q}\nu} = n_{\mathbf{q}\nu} \cdot \frac{\tilde{N}_{\mathbf{q}}}{N_{\mathbf{q}}} \tag{3.3}$$

The phonons excited in the calculation is given as $\tilde{n}_{\mathbf{q}\nu}$, which is equal to the number of phonons calculated without the rescaling multiplied with the fraction of the current number of grid points per axis ($\tilde{N}_{\mathbf{q}}$) and the default value for the grid points per axis ($N_{\mathbf{q}}$), which in this case is set to 200. The energies were found to be in much better agreement with each other, a small energy difference between the grid densities is still found at a scale of 0.00004%, which can be attributed to numerical noise.

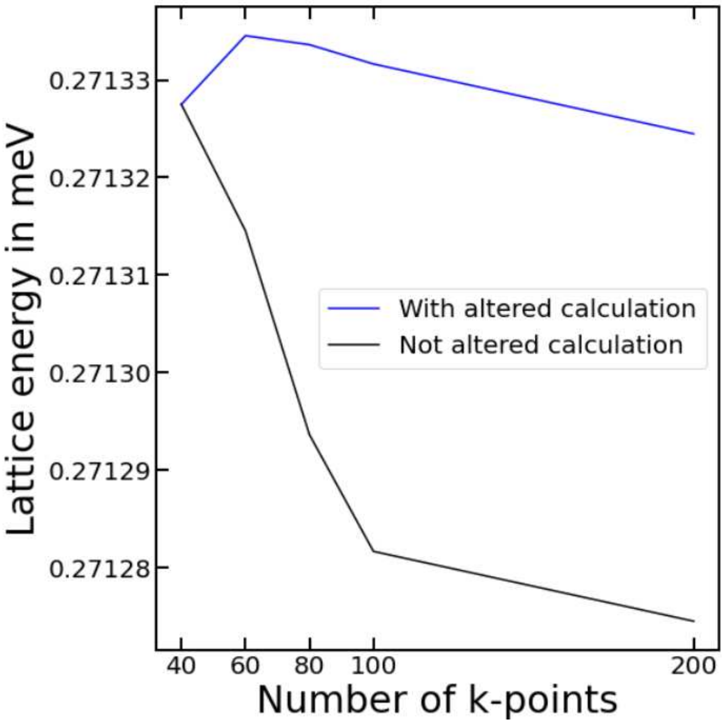

Figure 5: Lattice energies for different grid densities, before and after code modification.

In this work a number of properties is needed for the post-processing and analysis of the data. One output is not given with the original code, as the scattering rates of the phonon modes is calculated but not given out. This adjustment to the code is the last, and files containing the scattering rates at the last time step calculated are given out.

3.5 Broadening Parameter & Gaussian Smearing

The broadening parameter is a built-in variable of ShengBTE calculations. It has a default value of 1.0 and is the scale parameter for the Gaussian smearing of the data. This is required to approximate the delta function, by overlaying it with a Gaussian. The goal of the Gaussian smearing is to fill the data with noise in order to estimate the space between the calculated values without knowledge of the general shape of the values. The assumption that allows this treatment is a slowly varying density function. In the case of ShengBTE the calculations that use a small broadening ≤ 1.0 are significantly faster than calculations with a higher broadening parameter [50].

Smearing in ShengBTE is used to regulate the Dirac delta function through substitution by a finite-width approximation like the Gaussian function. This relaxes the strict restriction due to energy conservation. The wider the Gaussian function, the less strict the energy conservation is obeyed. Gaussian smearing can be seen as overlaying the calculated data-points with a Gaussian distribution, thus creating a continuous data set. The distribution in general is defined as:

$$g(x) = \frac{1}{\sigma\sqrt{w\pi}} \exp\left(-\frac{(x-\mu)^2}{2\sigma^2}\right) \tag{3.4}$$

The effect of the smearing can be tuned. The higher the smearing the more noise is brought into the data. In the case of ShengBTE the smearing can be controlled, by adjusting the parameter σ in Eq. 3.4. The smearing in ShengBTE is a special form of Gaussian smearing, as adaptive smearing is used here. If σ is too small there would not be enough phonon scattering channels. In the case of a value that is too large nonphysical scattering channels would be included in the calculation. This means that σ needs to be automatically changed to a desirable value for each part of reciprocal space around each q-point. The expression for σ used in the ShengBTE code is the following:

$$\sigma_W \approx \sqrt{\sum_\mu \left(\frac{\partial W}{\partial q'^\mu} \frac{\Delta q'^\mu}{\sqrt{12}}\right)^2} \tag{3.5}$$

This is used to calculate σ in ShengBTE. For this it is multiplied by an input given variable `scalebroad`. The lower this variable, the fewer three-phonon processes need to be considered. In the equation above q'^μ is the projection of the vector **q**' over the reciprocal-space vector $\mathbf{Q}_\mu$. W stands for the energy, that needs to be conserved in the calculations.

3.6 Convergence Tests

The challenge regarding the calculations is finding a compromise between the computational cost and the quality of the data calculated. Ideally a continuous grid would be introduced in the calculation, connecting each point in the simulated cell to a corresponding point in the simulation. This is virtually impossible to calculate however, so certain convergence tests need to be conducted in order to find the ideal parameters. First the quality of the data for different numbers of q-points used in the calculation is evaluated. The simulated cell is divided up into smaller cells, in the case of a $100 \times 100 \times 1$ grid the unit cell is cut into 10000 parts of equal size. The grid put onto the unit cell will be given as a single number, the grid mentioned before would be given as $q100$-grid. The smallest grid-size used is $q40$, the $q60$, $q80$ and $q100$ grids were also considered. In the later stages of the thesis a $q200$ grid is used for the full calculation, the calculation time needed is acceptable, given that the results were promising.

A first indicator for the quality of the calculation parameters is the temperature map of the unit cell. During the relaxation of the lattice certain patterns should emerge on these maps, highlighting the regions of higher or lower phonon scattering. In order to correctly observe and subsequently describe and explain these patterns they need to have as high a resolution as possible. In Fig. 6 such a plot can be seen, in this case a $q40$-grid is used for the calculation. There are certain parts in the plot where no value for a temperature can be taken, thus this grid density is not sufficient to describe the processes considered in the relaxation of the lattice, since the relevant patterns can not be evaluated with this resolution.

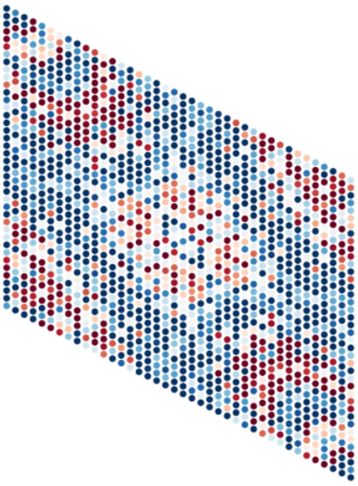

Figure 6: Temperature map for the q40 grid density, for the eighth phonon mode, after a time of 500fs.

A parameter that needs optimisation as well is the `scalebroad`-parameter, which - as explained in a subsection above - is a scaling parameter for the Gaussian smearing in ShengBTE. Optimising this parameter to balance the quality of the data and the calculation time yields the ideal value for this parameter in these calculations.

The higher the broadening parameter the smoother the data-set will appear when plotted. Nonetheless there is a limit to the value, as after a certain point the smearing will lead to a wrong representation of the data, due to the inclusion of nonphysical scattering channels. This scenario is to be avoided. Additionally the computational cost of a calculation with a higher broadening value increases rapidly above the default value of 1 [50].

The convergence tests for the broadening parameter start at the value of 0.5. For each value only one time-point will be calculated in order to enable a quick evaluation of the data. After the ideal set of parameters for the grid density and the broadening factor is found, a full calculation over 5ps can be started with a time-step of 0.001fs and a total of 5000 steps.

3.7 Phonon Relaxation & Grid Thermalisation

In order to be able to evaluate the phonon relaxation and grid thermalisation the output files of ShengBTE need to be post-processed. This is done via python scripts in jupyter. All of the plots in the this work were made through post-processing, if no source is mentioned. The first figure is the visualisation of the phonon dispersion. A successful Quantum Espresso calculation with converged phonon frequencies does not include any imaginary phonon frequencies, which would be visible as a negative frequency at the Γ-point in the phonon dispersion. If that is not the case the calculation has reached convergence and the phonon frequencies are correct. The frequencies are plotted over a path in reciprocal space, in this case the path is M-K-Γ-K'.

In order to evaluate the quality of the data the convergence tests are executed. In these mainly two plots are needed. One is the plot of the scattering rate over a certain path, which in this case is the Γ-K-M-K'-Γ path. As mentioned before, the smoother the graphs are, the better the data. The other is the plot of the temperature over a map of the simulated Brillouin zone. Here a distribution of the temperature that is as close to continuous as possible is looked for, this is a sign that the grid is sufficiently dense.

In order to evaluate the the scattering paths as well as the lattice thermalisation the phonon temperature superimposed to the phonon dispersion will be given. Here regions with a rising phonon population are visible by a heating of the specific point.

4 Results

In this section all the results of the work are presented. Starting with the basic equilibrium calculations of Quantum Espresso, to the simulation of the infrared Pump and the ShengBTE calculations. The numerical tests that lead to the ideal parameters of the ShengBTE calculations will also be presented, as well as the full scale calculation of phonon dynamics over a time of 5ps.

4.1 QE Results & IR Pump

The goal of the QE calculations is to set up the WS_2 structure for the subsequent calculations. To achieve this a self-consistent calculation of the relaxed solid structure is performed. The goal is achieved, if the calculation of the phonon dispersion showed no imaginary phonon frequencies, which is a common issue in QE calculations. Negative frequencies in the output imply imaginary phonon frequencies at the Γ-point, and this is not physical.

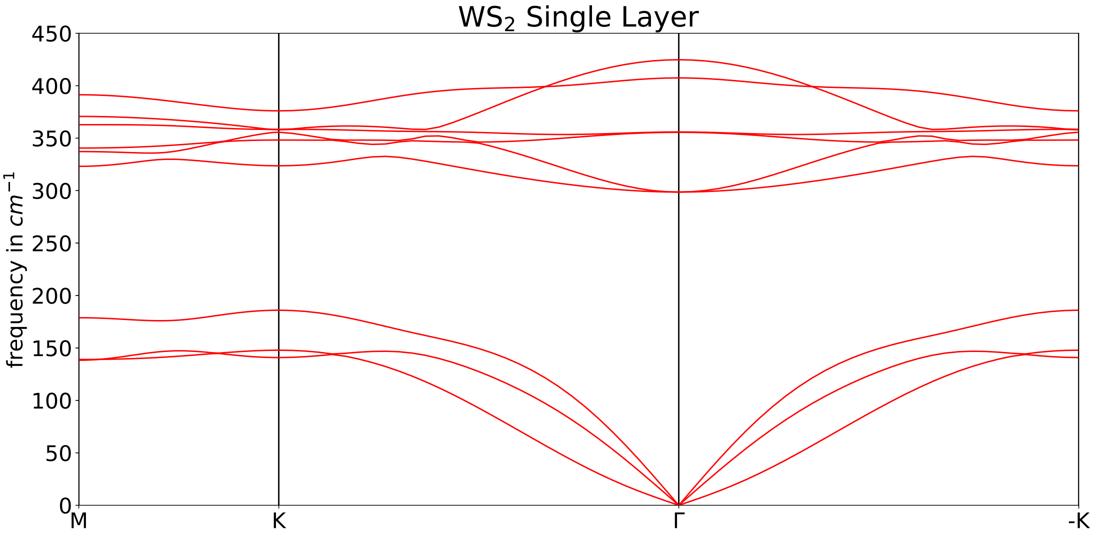

Figure 7: Phonon Dispersion of WS_2. At the Γ-point no negative phonon frequencies can be seen, the grid is converged.

In this case no imaginary phonon frequencies were found. This grid is the basis for all following calculations. First the effect of the IR pump needs to be investigated. As mentioned above an excitation through electromagnetic radiation in the infrared frequency range is used and the behaviour seen in Fig. 8 is expected.

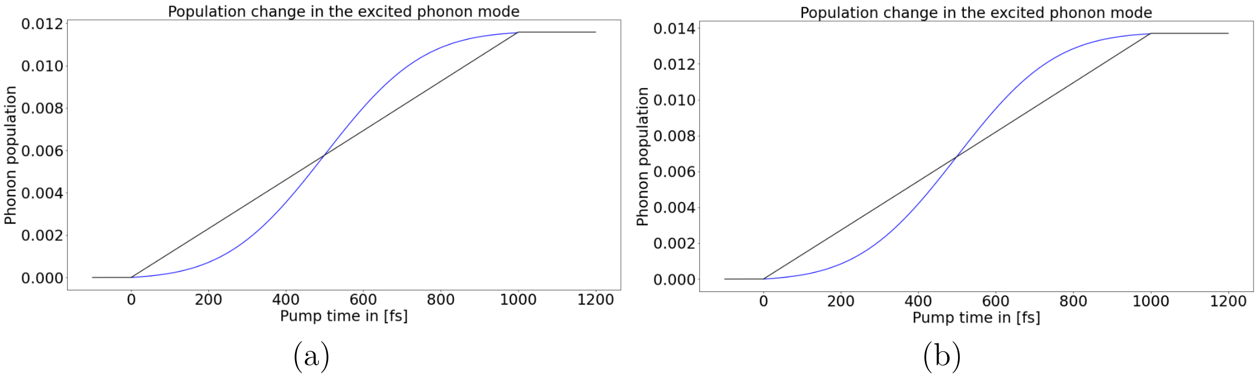

(a) (b)

Figure 8: Impact of the fluence on the phonon population. Panel (a) shows a fluence of 55[J/cm^2], in panel (b) the fluence was set to 65[J/cm^2].

The fluence has an impact on the increase in phonon population, as seen in the figure above. With a higher fluence the phonon population increases faster. Comparing the sides in Fig. 8, it can be seen that a higher phonon population is reached, within the same time for a higher fluence, for both the pump in a form of a Heaviside function in black and for the pump in form of a Gaussian in blue.
With the grid set up and the highest IR-active phonon mode excited the thermalisation can be calculated. Before this calculation can be started, a number of numerical tests needs to be performed in order to find the ideal set of parameters.

4.2 Numerical Tests

In the evaluation of the data from the calculations with different grid densities the smaller ones, from $q40$ up to $q80$ proved to have a very short calculation time of under seven hours for 1000 time steps with a step-length of 0.01fs. The data however is not convincing, as the grid is too loose, which can be seen by the plot of temperature of each grid section.

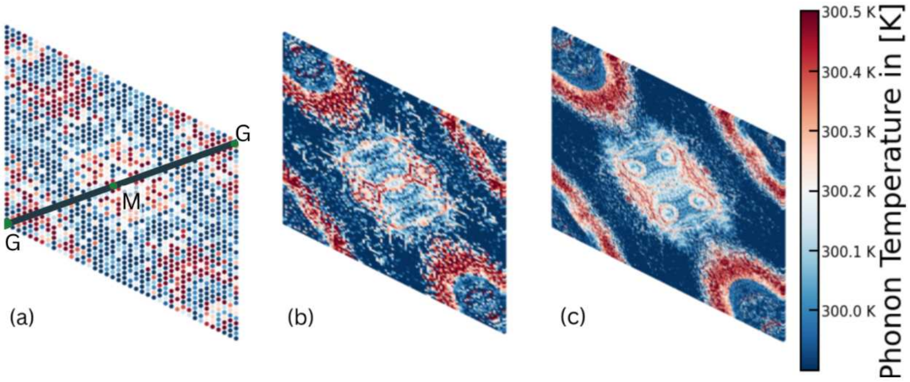

Figure 9: Plots of the temperature maps for different grid densities. In panel (a) the map for the q40 grid is shown. In panel (b) the map of the q100 grid is plotted, which already shows important features of the map, however in panel (c) for the q200 grid, these features are even clearer.

Smaller grid densities do not provide the best possibility to evaluate the thermalisation patterns. The patterns of relaxation can not be seen in detail, as no continuous temperature distribution is given. $q100$ is the first grid density with which the patterns can be evaluated. The denser the grid, the clearer the data, but a q200 grid is detailed enough to spot the relevant features, while also retaining a reasonable calculation time.
The calculations for the q100 and the q200 grids took approximately 12 hours, and 24 hours respectively. This number varies with the broadening parameter however. The higher the broadening is, the longer the calculations take. For a quick evaluation of the ideal grid density the broadening parameter is chosen to be rather low and the same for all the grid densities, at 0.5 broadening.
From the plots of the scattering rate in Fig. 9 it can be seen, that the denser grids provide a better scan of the path taken, which in this case is the Γ-K-M-K'-Γ path. A negative scattering rate suggests, that the phonon population decreases in the respective mode. In the case of an infinitely dense grid the plot of the scattering rate would have smooth curves without any harsh drops or spikes. This is due to the assumption, that the density function varies slowly, ruling out any sudden and extreme change in the scattering rate.

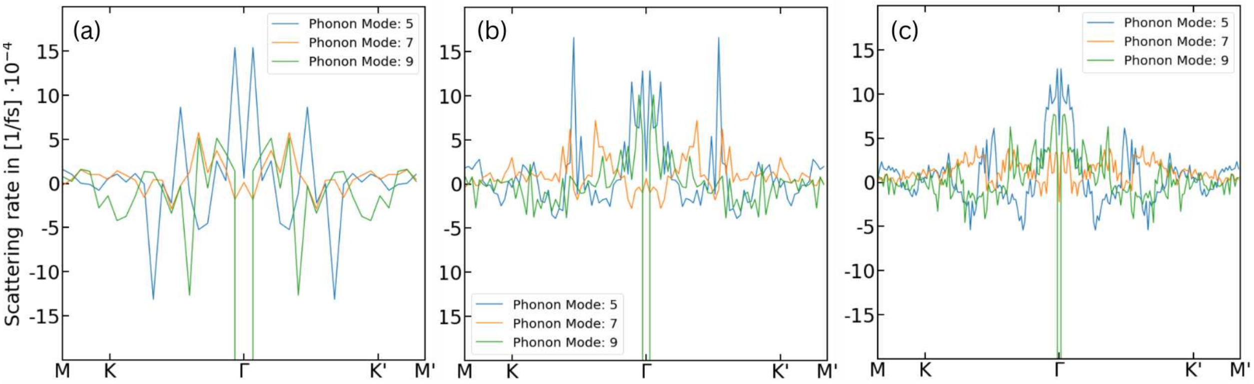

Figure 10: Comparison of the scattering rate for different grid densities. The figure reveals that the higher grid-densities move towards well defined graphs. In panel (a) the q40-grid is used, panel (b) shows the q100-grid, and panel (c) shows the q200-grid.

In Fig. 10 sharp spikes can be seen for all grid densities, for a selected number of phonon modes. Nonetheless the highest densities are acceptable, since the general shape of the scattering rate can be recognised. Another source of the rapid changes in scattering rate is the short time after the start of the thermalisation process calculated, which does not benefit the smoothness of the data, as for example in the case of the Γ-point an extremely negative scattering rate is expected, due to the excitation of the 9th phonon mode at $\mathbf{q} = 0$.
The plots are not ideal, which will be improved upon with the adjusted broadening parameter. This has been constant in the calculations up to now, at a value of 0.5. The broadening is the second and final value that will be optimised. As mentioned before the broadening is used for Gaussian smearing of the data in order to estimate the distribution of a continuous

grid without knowledge about the general shape of it.
The higher the broadening parameter, the more noise fills the gaps between the grid points. The default value in ShengBTE is 1.0. In the following the values 0.5, 1.0, 1.5 and 2.0 as well as 5.0 will be investigated. The goal is to represent the data as smooth as possible without misrepresenting it. Like before only one timestep is calculated. This is done for two reasons: the first is like before, the short time needed for this calculation. The second reason is that the important changes can already be seen after one timestep, which is important, as the higher broadening values increase the calculation time exponentially. The effect of the higher broadening can be seen in the following figures.

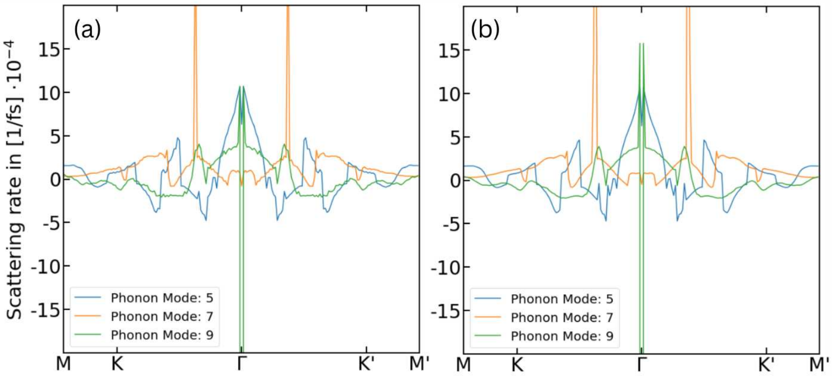

Figure 11: Effect of the broadening parameter. The case of broadening set to 0.5 is represented in the data before. Panel (a) shows a broadening factor 1.0. In panel (b) the plot for a broadening of 1.5 is shown. The simulation time increased by a factor of ~ 1.5.

The higher broadening shows smaller disturbances from the smooth curves. The change is significant with the broadening at 1.0. The best result however is seen for a broadening parameter of 1.5. Investigating the blue graph around the M-Point of the figure it can be seen, that the smoothness of the data could still be improved. Increasing the broadening parameter even more however is not beneficial, as the following plots for broadening factors of 2.0 and 5.0 show.

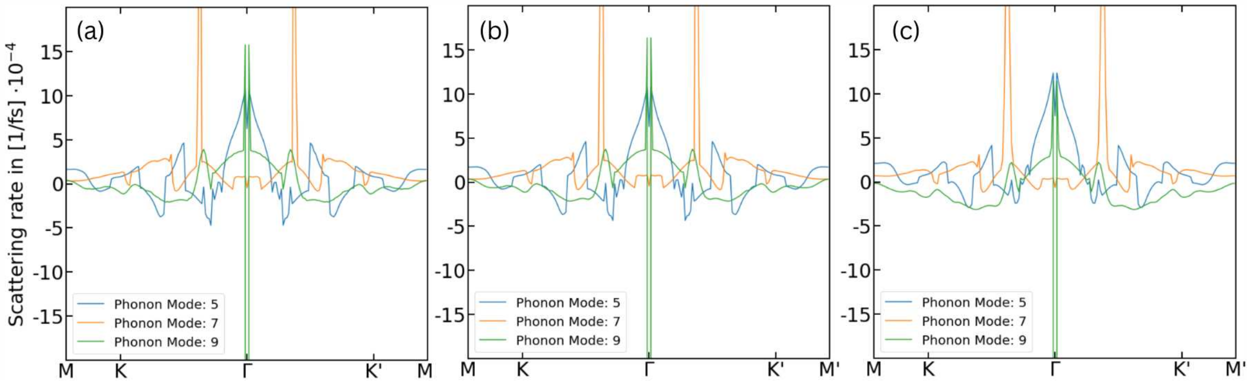

Figure 12: Impact of higher values for the broadening, seen by a shift in the scattering rates, which can be attributed to the inclusion of nonphysical scattering channels in the calculation.

An interesting effect can be seen in the figure above, especially in the transition from 2.0 to 5.0 the difference to the previous increase of the parameter is clearer. The same effect is also visible in the transition between 1.5 and 2.0, although it is of rather small magnitude here. In order to show the effect the calculation is done with 5.0 as well. What can be observed is a shift in the scattering rates with higher values for the broadening. This shift is not equal for all the phonon modes, as of the selected modes two experience a shift towards higher values while the remaining one is shifted towards lower values. Due to this the broadening values over 1.5 are not sensible options.

These findings set the final set of parameters at a grid density of $200 \times 200 \times 1$ k-points and a broadening of 1.5. With these inputs a new calculation is carried out, over 5000 time-steps with a length of 0.001fs each, resulting in a total simulated time of 5ps. This calculation takes ~ 11 days to complete. The results will be discussed below.

4.3 ShengBTE Results: Time Evolution

The time evolution of the excited system will be presented by the phonon temperature superimposed to the phonon dispersion seen before. With this representation the decay paths will be visible. The further into the red spectrum a colour is, the higher the temperature and the deeper into the blue hue, the lower the temperature of the phonon. In these figures a narrow range of temperature from 300.0K to 300.5K is chosen. The excited mode is set to a temperature of 6000K, but if the maximum temperature represented here would be the same, small variations which are be expected to occur especially early in the time evolution would not be observable. Apart from the excited mode in the highest available phonon branch at the Γ-point the phonon temperatures are set to 300K. The excited mode is set to a much higher temperature, the factor of 20 was chosen arbitrarily.

Fig. 13 shows the grid at the starting point. The highest available phonon mode is excited, as it is also the highest infrared active mode. This figure does not show the full grid, but an enlarged view of the excited phonon mode at the Γ-point. The excitation is visible by the dark red colour of the marker, which is placed to clarify the excitation. In general two principles need to be obeyed, the energy and the momentum need to be conserved. The path on which the data is calculated and visualised is the M-K-Γ-K'-M' path. Due to momentum conservation the phonons may only decay into states that obey the following equation: $\mathbf{q}_0 = \mathbf{q}_1 \pm \mathbf{q}_2$, with $\mathbf{q}_0$ being the decaying phonon, $\mathbf{q}_1$ and $\mathbf{q}_2$ the newly created phonons. With this it is clear that a symmetric phonon relaxation around the excited mode will be seen. The symmetry in the case of this work is given due to the $\mathbf{q} = 0$ point of the lattice being excited. The phonons have a momentum equal to 0, which in turn means that the two created phonons need to have the same momentum, with opposing signs. The symmetric patterns are expected over the whole simulation time.

In addition to the momentum conservation the energy of the decayed phonon needs to be

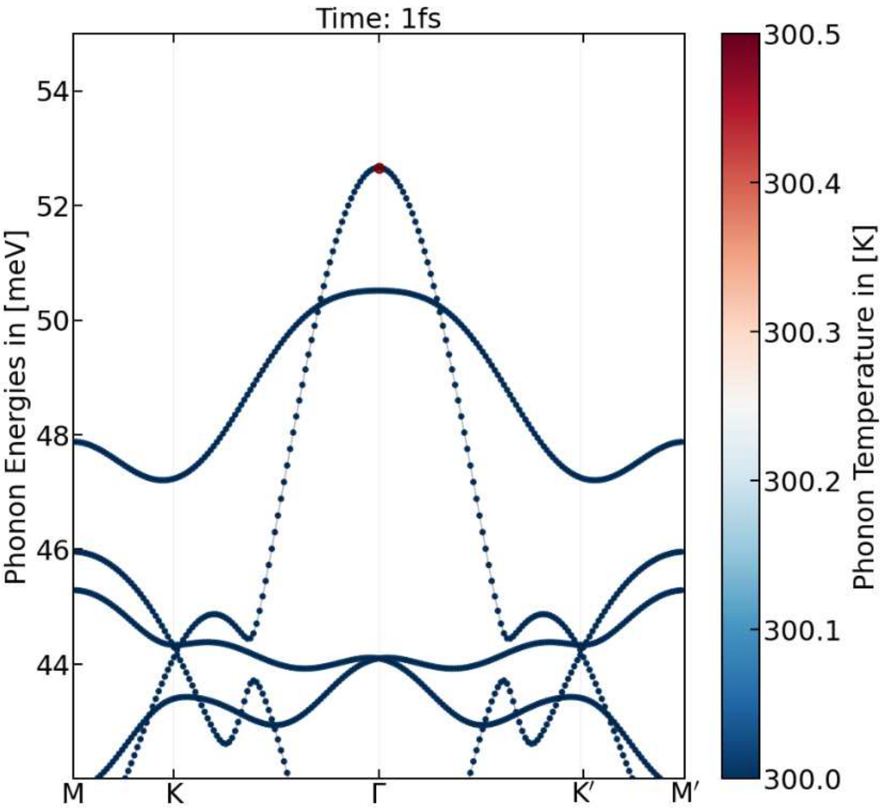

Figure 13: Phonon temperature superimposed to phonon dispersion, at the start of the calculation. The Excited mode is pointed out.

conserved. In general due to an excitation process phonons of a specific energy are excited, E_0. This energy needs to be conserved. If an optical phonon decays into two acoustic phonons by anharmonic interactions, the two energies combined need to be equal to E_0.
The first signs of scattering can be observed after around 250fs. Close to the Γ-point the population of the highest phonon mode relaxes symmetrically inside the mode into states with a $\mathbf{q}$ close to zero, obeying the momentum conservation. Additionally in the lowest optical mode a population increase in the region between the Γ and the K, and K' high-symmetry points can be observed. The phonon temperature is higher around the Γ-point than in the rest of the mode. A proof of energy conservation can not be seen in this figure. This is due to the limited choice of high symmetry points. In case of a consideration of the full Brillouin Zone and thus all high-symmetry points the heating of the corresponding phonon modes would be seen. In the case of the phonons close to the Γ-point of the lattice this will be seen after a longer simulated time period. Although not visible yet, the energy is conserved.
After 500fs a feature becomes more dominant. The LO^1 and TO^1 phonon branches are populated between the high symmetry points K and Γ, symmetrically also between K' and Γ. The heating of the mode in this specific point of the grid can be attributed to energetically preferred and available states, that the phonons scatter to. As a phonon of the population

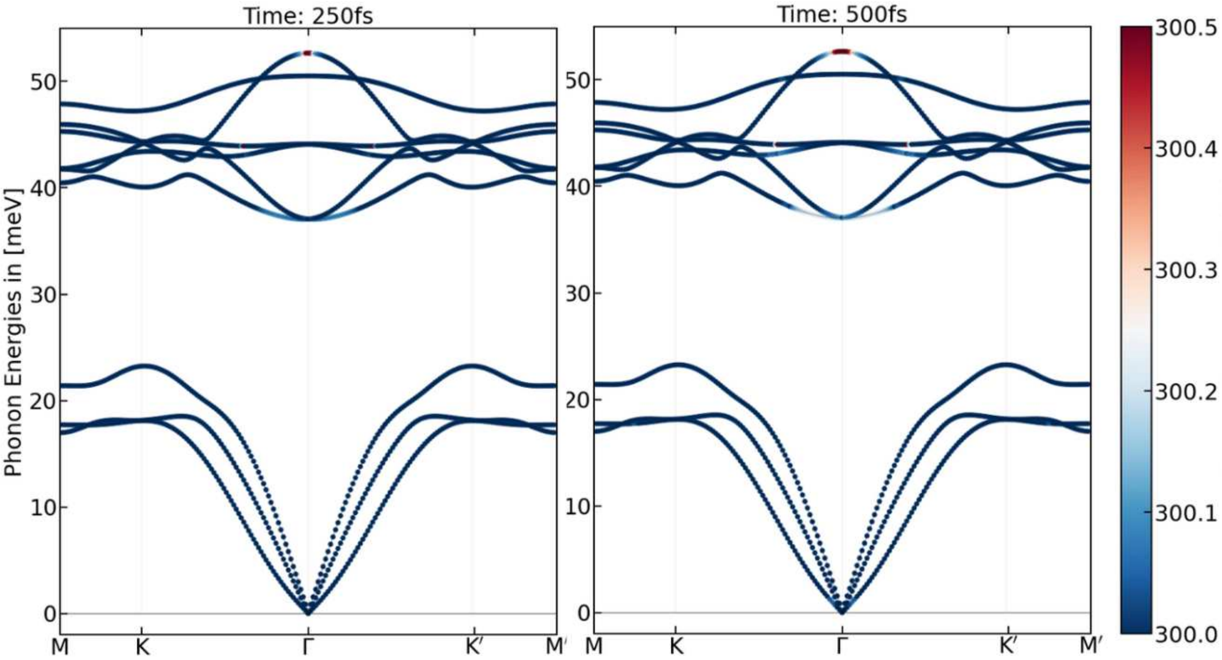

Figure 14: Phonon temperature superimposed to phonon dispersion. In (a), 250fs have passed, panel (b) depicts the lattice after 0.5ps.

excited before the start of the ShengBTE calculation decays the two resulting phonons split up the energy asymmetrically. One of the phonons has a higher energy and thus a higher frequency, appearing into an optical branch of the lattice. The other will be scattered into an acoustic branch.

This can be seen by the beginning heating of the ZA^1 mode, which is more easily visible in the figure that shows the lattice and temperature after 1fs. Close to the Γ-point a rising phonon population in the ZA^1 mode can be observed. Considering the Scattering process from the first step, this behaviour can be explained through energy conservation. The phonons from the originally excited mode decay, one phonon stays inside the same branch, with a different momentum. The other phonon therefore needs to be of a small energy. Thus a higher population around the Γ-point for the acoustic branches is expected. This is exactly what can be observed. An important factor that needs consideration are the opposing signs of the momenta. If for example a phonon decays and one of the resulting phonons scatters to the K-point of the lattice, the associated second phonon needs to scatter to the K'-point of the lattice.

The heating of the lowest acoustic phonon mode means the emergence of flexural phonons (FP) [51]. In graphene for example these phonons dominate the thermal conductivity. FP can be seen in the heating of the ZA acoustic mode. The presence of flexural phonons implies the vibration of the solid in the out of plane direction. Their influence on the properties of the crystal are subject to research [52, 53].

The flexural phonons are more easily visible in the next steps. The figure below shows a new region of heating. The LO^2 phonon branch heats at the intersection with the originally excited branch. This feature is more clearly visible after 2ps. Additionally a heating of the ZO^2 phonon branch can be observed around the intersection with the ZO^1 phonon branch. In the following time the aforementioned active regions still experience phonon scattering. The population of the branches increases and spreads symmetrically around the Γ-point.

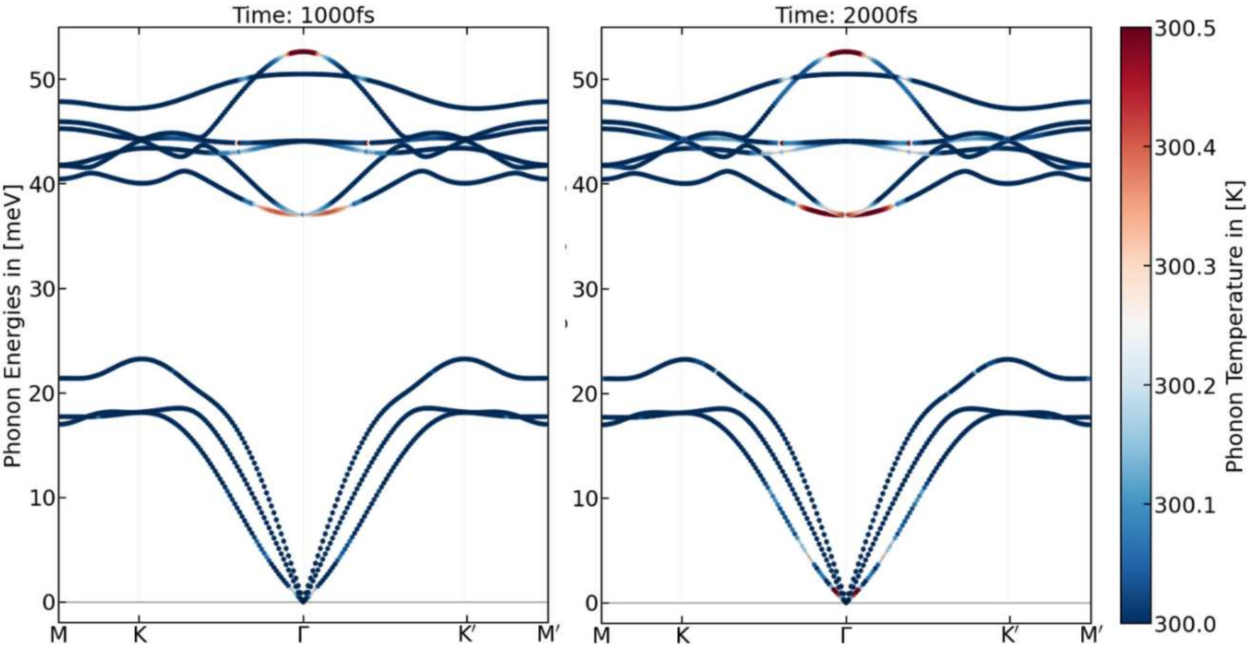

Figure 15: Phonon temperature superimposed to phonon dispersion. In (a), 1ps has passed, panel (b) depicts the lattice after 2ps.

Another process that begins to take shape is the heating of the phonons at the K and K' high-symmetry points of the lattice. This behaviour shows the momentum conservation. The energy conservation can not be verified, as the phonons may scatter to other points in the lattice, not depicted in these figures.

In the next steps a continuation of the already mentioned processes can be observed. A new feature is seen in the heating of the LA phonon mode between the Γ and the K point, or the K' point respectively, as seen in Fig. 16. Additionally the regions around the M and M' point are populated, for the highest optical and acoustic phonon branch at the M and M' points.

The 5000fs mark is the endpoint of the calculation. After 5ps the heating processes described above are still not complete. The Γ-point of the highest phonon mode is still highly populated, especially compared to the majority of the lattice. All phonon branches experience a rising phonon population at this point.

Fig. 16 depicts the final state of the phononic system. It is clear that the system is not completely thermalised. This would be the case if all phonon modes were equally populated, and thus thermal equilibrium would be found. In order to achieve this a calculation over a longer time period is needed. The first branch populated is the ZA[1] branch, which is the preferred mode of scattering from the originally excited mode at Γ-point.

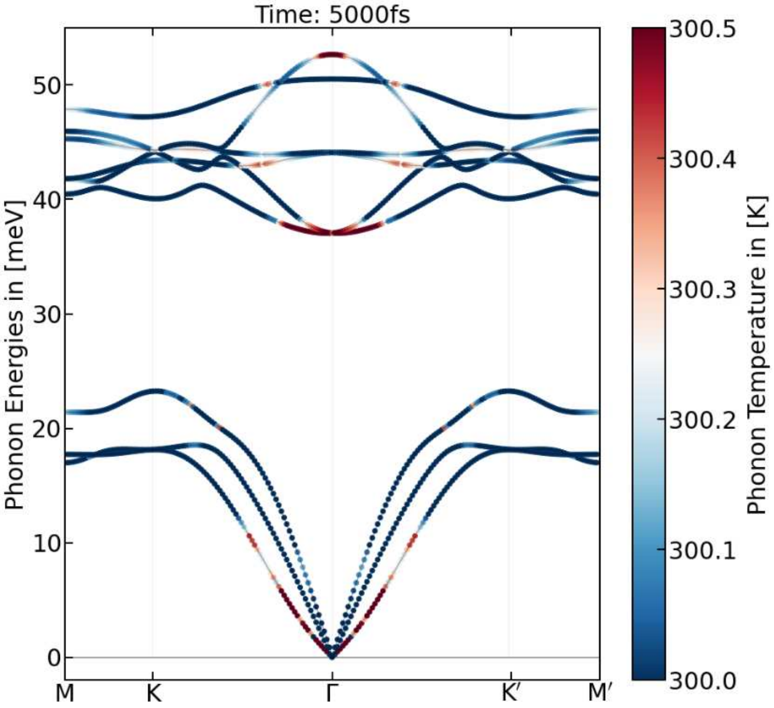

Figure 16: The lattice after 5ps, at the end of the calculation. Thermalisation is not achieved.

The preferred decay paths of the modes - especially at the start of the process - were clearly visible. A longer simulated time would be needed to achieve a fully thermalised lattice. The momentum conservation was verified over the whole calculation and the energy conservation is seen in an example. In order to verify the energy conservation completely a view over the whole Brillouin Zone would be needed.

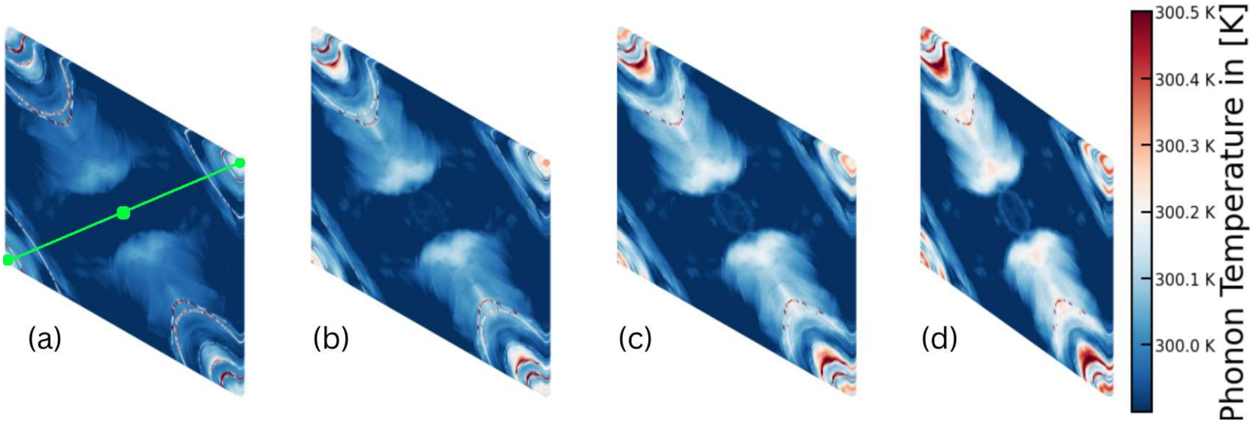

Figure 17: Average momentum resolved phonon temperature. In panel (a) the distribution after 1.25fs is shown, with high-symmetry points in green. (b) shows the lattice after 2.5fs, in (c) 3.75fs have passed. Panel (d) shows the final state, after 5ps.

Additionally to the previous figures a momentum-resolved temperature distribution over all phonon modes can be given. In the figure below the average phonon temperature of the lattice for different points in time is given.

In panel (a) in Fig. 17 the high-symmetry points Γ and M are given. Γ is shown twice, at the corners of the figure, M is the middle point. These visualisations are a possibility to access the tightly bonded high-symmetry points of the phonon scattering. If needed, this depiction can be altered to show all phonon modes individually. Additionally every step in the time-propagation can be visualised, leading to the possibility of representing the thermalisation of a given phonon mode in a variable time grid. This facilitates a variable data representation, with a modifiable density in time steps.

5 Conclusion & Outlook

In this thesis first principles calculations of THz driven polar semiconductors were carried out. In order to achieve this a variety of preliminary tests and calculations were carried out to achieve results that bear sufficient accuracy while also emphasising the efficiency of the calculation. In order to find the balance the codes were altered in specific important points and a number of convergence tests were performed, to find the ideal parameters for the calculation.

First the structure of Tungsten-Di-sulphide was calculated using Quantum Espresso. The structure was relaxed and the phonon dispersion was calculated. A common issue with Quantum Espresso calculations was avoided, as the phonon frequencies of the acoustic branches at the Γ-point did not take on negative values, indicating imaginary frequencies.

As a second step the ShengBTE calculations were altered to suit the needs for this calculation. Originally the code is used to calculate equilibrium states. Here a non-equilibrium state was needed. Additionally a correction of the number of excited phonons was introduced, to compare the quality of different setups. The calculations in this work were a result of the process of adjusting the simulation codes to facilitate the calculations as wished. After completing this process the evaluation of the time propagation of the phonon temperatures superimposed to the previously calculated phonon dispersion was possible.

In the evaluation of the data the dominant paths of thermalisation of WS_2 were found and the relaxation of the lattice was observed, with the principles of energy and momentum conservation in mind. The latter of which was clearly observable. Concerning the energy conservation further simulation is needed, especially the inclusion of more high symmetry points would lead to a better possibility for confirmation.

A procedure was defined with which the set up for calculations like the ones in this work can be carried out. For this the simulation code was altered to fit the requirements. One procedure of major importance is the evaluation of the ideal simulation parameters. The process is transferable for other crystalline solids.

The thermalisation of a previously excited lattice was calculated and analysed with a variety of visualisation possibilities providing insight into the processes at hand. Temperature distributions over the phonon dispersion paint a detailed picture of the thermalisation of the lattice. The momentum resolved temperature maps show the distribution of the temperature and with it the lattice energy in **q**-space, enabling the investigation of preferred scattering paths.

This is one of the possible directions for future research on this topic. A wide variety of systems can be calculated using the same procedure and with a longer timescale of simulation a full thermalisation from a non-equilibrium state can be carried out.

Literaturverzeichnis

[1] J. M. Ziman. *Electrons and Phonons: The Theory of Transport Phenomena in Solids.* Oxford University Press, 1960.

[2] D.A. Broido et al. Intrinsic lattice thermal conductivity of semiconductors from first principles. *Applied Physics Letters*, 91, 2007.

[3] M. Zebarjadi et al. Perspectives on thermoelectrics: from fundamentals to device applications. *Energy Environ. Sci.*, 5:5147–5162, 2012.

[4] Jagdeep Shah. *Ultrafast Spectroscopy of Semiconductors and Semiconductor Nanostructures.* Springer Berlin, Heidelberg, 1999.

[5] Xiao Tong and Marco Bernardi. Toward precise simulations of the coupled ultrafast dynamics of electrons and atomic vibrations in materials. *Phys. Rev. Research*, 3:023072, Apr 2021.

[6] Fabio Caruso. Nonequilibrium lattice dyamics in monolayer mos2. *The Journal of Physical Chemistry Letters*, 12(6):1734–1740, 2021.

[7] Marco Bernardi. First-principles dynamics of electrons and phonons, 2016.

[8] Vatsal A. Jhalani et al. Ultrafast hot carrier dynamics in gan and its impact on the efficiency droop. *Nano Letters*, 17(8):5012–5019, 2017.

[9] Surbhi Lal, Stephan Link, and Naomi J. Halas. Nano-optics from sensing to waveguiding. *Nature Photonics*, 1:641–648, 2007.

[10] B. Radišavljević et al. Single-layer mos2 transistors. *Nature Nanotechnology*, 6, 2011.

[11] Wonbong Choi et al. Recent development of two-dimensional transition metal dichalcogenides and their applications. *Materials Today*, 20:116–130, 2017.

[12] Shaswat Barua et al. Nanostructured mos2-based advanced biosensors: A review. *ACS Applied Nano Materials*, 1, 2018.

[13] Yongfeng Sun et al. Tribological performance of a tungsten disulfide lubricant film prepared by atomic layer deposition using tungsten hexacarbonyl and hydrogen sulfide as preursors. *Tribology International*, 114:478–484, 2017.

[14] S.V Prasad et al. Tribology of tungsten disulfide-nanocrystalline zinc oxide adaptive lubricant films from ambient to 500° c. *Wear*, 237:186–196, 2000.

[15] Michele Buzzi et al. Probing dynamics in quantum materials with femtosecond x-rays. *Nature Reviews Materials*, 3, 2018.

[16] Ebrahim Najafi, Vsevolod Ivanov, Ahmed Zewail, and Marco Bernardi. Super-diffusion of excited carriers in semiconductors. *Nature Communications*, 8, 5 2017.

[17] L Young et al. Femtosecond electronic response of atoms to ultra-intense x-rays. *Nature*, 466, 2010.

[18] Kunie Ishioka et al. *Coherent Lattice Oscillations in Solids and Their Optical Control*, pages 47–63. Springer Berlin, Heidelberg, 2010.

[19] R. Mankowsky, A. von Hoegen, M. Först, and A. Cavalleri. Ultrafast reversal of the ferroelectric polarization. *Phys. Rev. Lett.*, 118:197601, May 2017.

[20] Giovanni Onida, Lucia Reining, and Angel Rubio. Electronic excitations: density-functional versus many-body green's-function approaches. *Rev. Mod. Phys.*, 74:601–659, Jun 2002.

[21] Miguel A.L. Marques et al. Octopus: a first-principles tool for excited electron–ion dynamics. *Computer Physics Communications*, 151:60–78, 2003.

[22] Alberto Castro et al. Propagators for the time-dependent kohn-sham equations. *The Journal of Chemical Physics*, 121:3425–3433, 2004.

[23] W. Kohn and L. J. Sham. Self-consistent equations including exchange and correlation effects. *Phys. Rev.*, 140:A1133–A1138, Nov 1965.

[24] Fabio Caruso and Dino Novko. Ultrafast dynamics of electrons and phonons: from the two-temperature model to the time-dependent boltzmann equation, 2022.

[25] E. Schrödinger. An undulatory theory of the mechanics of atoms and molecules. *Phys. Rev.*, 28:1049–1070, Dec 1926.

[26] M. Born and R. Oppenheimer. Zur quantentheorie der molekeln. *Annalen der Physik*, 389(20):457–494, 1927.

[27] P. Hohenberg and W. Kohn. Inhomogeneous electron gas. *Phys. Rev.*, 136:B864–B871, Nov 1964.

[28] Gabriele Giuliani, Giovanni Vignale, and Erio Tosatti. Quantum theory of the electron liquid. *Physics Today - PHYS TODAY*, 59, 10 2006.

[29] Giuseppe Grosso and Giuseppe Parravicini. *Solid State Physics*, pages 1–727. Academic Press, London, 2000.

[30] Feliciano Giustino. Electron-phonon interactions from first principles. *Rev. Mod. Phys.*, 89:015003, Feb 2017.

[31] Richard M. Martin. *Electronic Structure.* Cambridge University Press, 2004.

[32] Ossama El Abouti et al. Comparison of brillouin light scattering and density of states in a supported layer: Analytical and experimental study. *Crystals*, 12, 2022.

[33] N. Troullier and José Luís Martins. Efficient pseudopotentials for plane-wave calculations. *Phys. Rev. B*, 43:1993–2006, Jan 1991.

[34] David Singh and Lars Nordström. *Planewaves, Pseudopotentials and the LAPW Method, Second Edition.* Springer New York, NY, 12 2005.

[35] S. Goedecker and K. Maschke. Transferability of pseudopotentials. *Phys. Rev. A*, 45:88–93, Jan 1992.

[36] Warren E. Pickett. Pseudopotential methods in condensed matter applications. *Computer Physics Reports*, 9(3):115–197, 1989.

[37] David Vanderbilt. Soft self-consistent pseudopotentials in a generalized eigenvalue formalism. *Phys. Rev. B*, 41:7892–7895, Apr 1990.

[38] G. B. Bachelet, D. R. Hamann, and M. Schlüter. Pseudopotentials that work: From h to pu. *Phys. Rev. B*, 26:4199–4228, Oct 1982.

[39] Baldassare Di Bartolo and Richard C. Powell. *Crystal Symmetry, Lattice Vibrations, and Optical Spectroscopy of Solids.* World Scientific, 2014.

[40] Peter Brüesch. *Phonons: Theory and Experiments II.* Springer, 1986.

[41] Mark Fox. *Optical Properties of Solids.* American Journal of Physics, 2002.

[42] J. Hohlfeld et al. Electron and lattice dynamics following optical excitation of metals. *Chemical Physics*, 251(1):237–258, 2000.

[43] L. D. Landau and L. M. Lifshitz. *Quantum Mechanics Non-Relativistic Theory, Third Edition: Volume 3.* Butterworth-Heinemann, 3 edition, 1981.

[44] David Pines and J. Robert Schrieffer. Approach to equilibrium of electrons, plasmons, and phonons in quantum and classical plasmas. *Phys. Rev.*, 125:804–812, Feb 1962.

[45] Jinzi Ding et al. Properties, preparation, and application of tungsten disulfide: a review. *Journal of Physics D: Applied Physics*, 54:173002, Feb 2021.

[46] Ali Eftekhari. Directed energy transfer from monolayer ws2 to near-infrared emitting pbs-cds quantum dots. *J. Mater. Chem. A*, 5:18299–18325, 2017.

[47] A. Rycerz et al. Valley filter and valley valve in graphene. *Nature Physics*, 3, 2007.

[48] Xin Zhang et al. Phonon and raman scattering of two-dimensional transition metal dichalcogenides from monolayer, multilayer to bulk material. *Chem. Soc. Rev.*, 44:2757–2758, 2015.

[49] Se-Yang Kim et al. Recent developments in controlled vapor-phase growth of 2d group 6 transition metal dichalcogenides. *Advanced Materials*, 31, 2019.

[50] Documentation for shengbte. `https://bitbucket.org/sousaw/shengbte/src/master/README.md`. Date: 22.11.22.

[51] Chenmu Zhang, Long Cheng, and Yuanyue Liu. Role of flexural phonons in carrier mobility of two-dimensional semiconductors: Free standing vs on substrate. *Journal of Physics: Condensed Matter*, 33, 02 2021.

[52] Thibault Sohier, Matteo Calandra, and Francesco Mauri. Density functional perturbation theory for gated two-dimensional heterostructures: Theoretical developments and application to flexural phonons in graphene. *Phys. Rev. B*, 96:075448, Aug 2017.

[53] Massimo V. Fischetti and William G. Vandenberghe. Mermin-wagner theorem, flexural modes, and degraded carrier mobility in two-dimensional crystals with broken horizontal mirror symmetry. *Phys. Rev. B*, 93:155413, Apr 2016.

List of Figures

Acknowledgements

I would like to thank Prof. Dr. Fabio Caruso, the first evaluator and my academic advisor, for guiding me through the thick forest of solid-state physics. I also want to thank Prof. Dr. Michael Bauer, the second evaluator of this thesis for fuelling my interest in solid state-physics. A special thanks goes to Chris, who helped me both in a personal and academic sense, as well as Yiming, Phillip and Melina, for our fruitful discussions, both on- and off-topic. Last but not least, I want to thank my family. Your support means the world to me.

Erklärung

Name: Ćapin
Vorname: Mate
Matrikelnummer: 1112086

Erklärung gemäß Paragraph 9 Absatz 7 der Prüfungsverfahrensordnung der Christian-Albrechts-Universität zu Kiel für Studierende der Bachelor- und Master-Studiengänge.

Hiermit erkläre ich, dass ich die Arbeit selbstständig verfasst und keine anderen als die angegebenen Quellen und Hilfsmittel benutzt und die Arbeit in keinem anderen Prüfungsverfahren eingereicht habe.

Datum & Unterschrift: ______________________________